von Karman Institute for Fluid Dynamics

Lecture Series 1990–03

COMPUTATIONAL FLUID DYNAMICS

March 5–9, 1990

TOWARDS A GENUINELY MULTI-DIMENSIONAL UPWIND SCHEME

K.G. Powell, B. van Leer, P.L. Roe

U. Michigan, USA

Towards a Genuinely Multi-Dimensional Upwind Scheme

Kenneth G. Powell, Bram van Leer and Philip L. Roe
Department of Aerospace Engineering
The University of Michigan
Ann Arbor, Michigan USA

March, 1990

1 Abstract

Several methods of incorporating multi-dimensional ideas into algorithms for the solution of the Euler equations are presented and discussed. Three schemes are developed and tested; a scheme based on a downwind distribution, a scheme based on a rotated Riemann solver and a scheme based on a generalized Riemann solver. The schemes all show a marked improvement over first-order, grid-aligned upwind schemes, but the higher-order performance is less impressive. An outlook for the future of multi-dimensional upwind schemes is given.

2 Introduction

2.1 The 1D Euler Equations

The Euler equations of gasdynamics express the conservation of mass, momentum and energy for a continuous, non-conducting inviscid fluid. In one dimension, they may be written

$$\frac{\partial \mathbf{u}}{\partial t} + \frac{\partial \mathbf{f}}{\partial x} = 0\,, \tag{1a}$$

where $\mathbf{u}$ is the 'state vector,' the vector of conserved quantities,

$$\mathbf{u} = \left\{ \begin{array}{c} \rho \\ \rho u \\ \rho E \end{array} \right\}, \tag{1b}$$

and $\mathbf{f}$ is the 'flux vector,' given by

$$\mathbf{f} = \left\{ \begin{array}{c} \rho u \\ \rho u^2 + p \\ \rho u h_0 \end{array} \right\} . \tag{1c}$$

The ideal gas relation

$$\frac{p}{\rho} = (\gamma - 1) \left[E - \frac{u^2}{2} \right] \tag{1d}$$

and the definition of total enthalpy

$$h_0 = \left(E + \frac{p}{\rho} \right) \tag{1e}$$

close the set of equations.

The primitive variable form of the equations may also be written in vector form, giving

$$\frac{\partial \tilde{\mathbf{u}}}{\partial t} + \tilde{\mathbf{a}} \frac{\partial \tilde{\mathbf{u}}}{\partial x} = 0 , \tag{2a}$$

where $\tilde{\mathbf{u}}$ is the vector of primitive variables

$$\tilde{\mathbf{u}} = \left\{ \begin{array}{c} \rho \\ u \\ p \end{array} \right\} \tag{2b}$$

and $\tilde{\mathbf{a}}$ is the Jacobian matrix

$$\tilde{\mathbf{a}} = \left[\begin{array}{ccc} u & \rho & 0 \\ 0 & u & \frac{1}{\rho} \\ 0 & \rho c^2 & u \end{array} \right] . \tag{2c}$$

Travelling wave solutions to the one-dimensional Euler equations may be sought by substituting

$$\tilde{\mathbf{u}}(x,t) = \tilde{\mathbf{u}}(x - \lambda t) \tag{3a}$$

into Equation 2a, giving the eigenvalue problem

$$(\tilde{\mathbf{a}} - \lambda \mathbf{I}) \, \delta\tilde{\mathbf{u}} = 0 , \tag{3b}$$

where $\mathbf{I}$ is the three by three identity matrix, and $\delta\tilde{\mathbf{u}}$ is the amplitude of the traveling wave. The solution of this problem depends upon the eigenvalues and eigenvectors of $\tilde{\mathbf{a}}$ described below.

First Acoustic Wave

The eigenvalue

$$\lambda = u - c \tag{4a}$$

and corresponding right eigenvector

$$\tilde{\mathbf{r}}_1 = \begin{Bmatrix} \rho \\ -c \\ \rho c^2 \end{Bmatrix} \tag{4b}$$

represent an acoustic disturbance. The wave travels with the fluid velocity minus the speed of sound.

Entropy Wave

The eigenvalue

$$\lambda = u \tag{4c}$$

and corresponding eigenvector

$$\tilde{\mathbf{r}}_2 = \begin{Bmatrix} \rho \\ 0 \\ 0 \end{Bmatrix} \tag{4d}$$

represent a change in density with no corresponding change in pressure, and can be thought of as an entropy wave. The wave travels with the fluid velocity, as can be seen from the eigenvalue.

Second Acoustic Wave

The eigenvalue

$$\lambda = u + c \tag{4e}$$

and corresponding right eigenvector

$$\tilde{\mathbf{r}}_3 = \begin{Bmatrix} \rho \\ c \\ \rho c^2 \end{Bmatrix} \tag{4f}$$

also represent an acoustic disturbance. The wave travels with the fluid velocity plus the speed of sound.

The "characteristic variables" are given by

$$d\mathbf{w} = \tilde{\mathbf{r}}^{-1} \delta \tilde{\mathbf{u}} \tag{5a}$$

$$= \left\{ \begin{array}{c} \frac{1}{2}\left[\frac{\delta p}{\rho c^2} - \frac{\delta u}{c}\right] \\ \frac{\delta \rho}{\rho} - \frac{\delta p}{\rho c^2} \\ \frac{1}{2}\left[\frac{\delta p}{\rho c^2} + \frac{\delta u}{c}\right] \end{array} \right\} . \tag{5b}$$

Modern schemes for compressible flow are based on these travelling wave solutions to the one-dimensional Euler equations. The Euler equations in their conservative form (Equation 1a) are integrated over cell number i, which extends from cell-face $i - 1/2$ to cell-face $i + 1/2$. This gives

$$\int_{i-\frac{1}{2}}^{i+\frac{1}{2}} \frac{\partial \mathbf{u}}{\partial t}\, dx + \int_{i-\frac{1}{2}}^{i+\frac{1}{2}} \frac{\partial \mathbf{f}}{\partial x}\, dx = 0 \tag{6a}$$

Defining the cell-average state vector $\bar{\mathbf{u}}$ and applying Gauss' theorem gives

$$\frac{\partial \bar{\mathbf{u}}}{\partial t} + \left(\mathbf{f}_{i+\frac{1}{2}} - \mathbf{f}_{i-\frac{1}{2}}\right) = 0 \tag{6b}$$

where $\mathbf{f_{i+1/2}} = \mathbf{f}(\mathbf{u_L}, \mathbf{u_R})$ is a "numerical flux function," constructed so that the components of $d\mathbf{w}$ for which λ is positive (corresponding to a wave travelling in the positive x direction) are backward differenced, and the components for which λ is negative (corresponding to a wave moving in the negative x direction) are forward differenced. In the above, $\mathbf{u_L}$ and $\mathbf{u_R}$ are values of the state vector just to the left and right sides of the interface, respectively. These can be taken to be equal to the nearest cell center values, yielding a first-order scheme, or obtained by some interpolation of the cell-center values, yielding a higher-order scheme. An outline of several of the flux functions currently in use has been given by Van Leer *et al* [1].

The schemes outlined in this paper are primarily based on the flux function of Roe [2]. For this flux function, the "Roe-average" of the states $\tilde{\mathbf{u}}_\mathbf{L}$ and $\tilde{\mathbf{u}}_\mathbf{R}$ is defined, with

$$\hat{\rho} = \left(\frac{1}{\rho_L} w + \frac{1}{\rho_R}(1-w)\right)^{-1} , \tag{7a}$$

$$\hat{u} = u_L w + u_R (1-w) , \tag{7b}$$

$$\hat{h}_0 = h_{0_L} w + h_{0_R} (1-w) , \tag{7c}$$

$$\hat{c} = \sqrt{(\gamma - 1)\left[\hat{h}_0 - \frac{1}{2}\hat{u}^2\right]} ; \tag{7d}$$

where

$$w = \frac{\sqrt{\rho_L}}{\sqrt{\rho_L} + \sqrt{\rho_R}} . \tag{7e}$$

The interface flux is then defined as

$$\mathbf{f}(\mathbf{u_L}, \mathbf{u_R}) = \frac{1}{2}(\mathbf{f_L} + \mathbf{f_R}) - \frac{1}{2}\sum_{k=1}^{3} \left|\hat{\lambda}_k\right| \Delta V_k \hat{\mathbf{r}}_k , \tag{8}$$

with $\hat{\mathbf{r}}_k$, $\hat{\lambda}_k$ and ΔV_k as given below:

$$\hat{\mathbf{r}}_1 = \begin{pmatrix} 1 \\ \hat{u} - \hat{c} \\ \hat{h}_0 - \hat{u}\hat{c} \end{pmatrix}, \tag{9a}$$

$$\hat{\mathbf{r}}_2 = \begin{pmatrix} 1 \\ \hat{u} \\ \frac{\hat{u}^2}{2} \end{pmatrix}, \tag{9b}$$

$$\hat{\mathbf{r}}_3 = \begin{pmatrix} 1 \\ \hat{u} + \hat{c} \\ \hat{h}_0 + \hat{u}\hat{c} \end{pmatrix}; \tag{9c}$$

$$\Delta \mathbf{V} = \begin{pmatrix} \frac{1}{2\hat{c}^2}\left(\Delta p - \hat{\rho}\hat{c}\Delta u\right) \\ -\frac{1}{\hat{c}^2}\left(\Delta p - \hat{c}^2 \Delta \rho\right) \\ \frac{1}{2\hat{c}^2}\left(\Delta p + \hat{\rho}\hat{c}\Delta u\right) \end{pmatrix}; \tag{10}$$

$$\lambda_1 = \hat{u} - \hat{c}, \tag{11a}$$

$$\lambda_2 = \hat{u}, \tag{11b}$$

$$\lambda_3 = \hat{u} + \hat{c}. \tag{11c}$$

As with the quasilinear form, the $\hat{\mathbf{r}}_k$'s can be interpreted as waves of strength ΔV_k, propagating with speed λ_k. Here, the subscript 1 denotes the first acoustic wave, the subscript 2 denotes the entropy wave and the subscript 3 the second acoustic wave.

2.2 The 2D Euler Equations

In two dimensions, the Euler equations may be written as

$$\frac{\partial \mathbf{U}}{\partial t} + \frac{\partial \mathbf{F}}{\partial x} + \frac{\partial \mathbf{G}}{\partial y} = 0, \tag{12a}$$

where $\mathbf{U}$ is the state vector,

$$\mathbf{U} = \left\{ \begin{array}{c} \rho \\ \rho u \\ \rho v \\ \rho E \end{array} \right\}, \tag{12b}$$

and $\mathbf{F}$ and $\mathbf{G}$ are the flux vectors, given by

$$\mathbf{F} = \left\{ \begin{array}{c} \rho u \\ \rho u^2 + p \\ \rho uv \\ \rho u h_0 \end{array} \right\} \qquad \mathbf{G} = \left\{ \begin{array}{c} \rho v \\ \rho uv \\ \rho v^2 + p \\ \rho v h_0 \end{array} \right\}. \tag{12c}$$

The ideal gas relation for the two-dimensional case is

$$\frac{p}{\rho} = (\gamma - 1)\left[E - \frac{u^2 + v^2}{2}\right]. \tag{12d}$$

The Euler equations may also be written in the quasilinear form

$$\frac{\partial \tilde{\mathbf{U}}}{\partial t} + \tilde{\mathbf{A}}\frac{\partial \tilde{\mathbf{U}}}{\partial x} + \tilde{\mathbf{B}}\frac{\partial \tilde{\mathbf{U}}}{\partial y} = 0, \tag{13a}$$

where $\tilde{\mathbf{A}}$ and $\tilde{\mathbf{B}}$ are the Jacobian matrices

$$\tilde{\mathbf{A}} = \begin{bmatrix} u & \rho & 0 & 0 \\ 0 & u & 0 & \frac{1}{\rho} \\ 0 & 0 & u & 0 \\ 0 & \rho c^2 & 0 & u \end{bmatrix} \tag{13b}$$

and

$$\tilde{\mathbf{B}} = \begin{bmatrix} v & 0 & \rho & 0 \\ 0 & v & 0 & 0 \\ 0 & 0 & v & \frac{1}{\rho} \\ 0 & 0 & \rho c^2 & v \end{bmatrix}, \tag{13c}$$

and $\tilde{\mathbf{U}}$ is the vector of primitive variables

$$\tilde{\mathbf{U}} = \begin{Bmatrix} \rho \\ u \\ v \\ p \end{Bmatrix} . \tag{13d}$$

Travelling wave solutions to the two-dimensional Euler equations are of the form

$$\tilde{\mathbf{U}}(x, y, t) = \tilde{\mathbf{U}}(x\kappa_x + y\kappa_y - \lambda t) \tag{14a}$$

where $\boldsymbol{\kappa} = \kappa_x \mathbf{e_x} + \kappa_y \mathbf{e_y}$ is a unit vector in the direction of propagation. Substituting this form of solution into Equation 13a gives the eigenvalue problem

$$\left(\tilde{\mathbf{A}}\kappa_x + \tilde{\mathbf{B}}\kappa_y - \lambda \mathbf{I}\right) \delta\tilde{\mathbf{U}} = 0 , \tag{14b}$$

where $\mathbf{I}$ is the four by four identity matrix, and $\delta\tilde{\mathbf{U}}$ is the amplitude of the traveling wave. This deceptively simple-looking equation is much more complex than its one-dimensional counterpart.

The matrix $\tilde{\mathbf{R}}$ is made up of the right eigenvectors of the matrix $\tilde{\mathbf{A}}\kappa_x + \tilde{\mathbf{B}}\kappa_y$. The four eigenvectors and their corresponding eigenvalues are as follows.

First Acoustic Wave

The eigenvalue

$$\lambda = u\kappa_x + v\kappa_y - c \tag{15a}$$

and corresponding right eigenvector

$$\tilde{\mathbf{R}}_1 = \begin{Bmatrix} \rho \\ -c\kappa_x \\ -c\kappa_y \\ \rho c^2 \end{Bmatrix} \tag{15b}$$

represent an acoustic disturbance. The wave travels with the projected fluid velocity minus the speed of sound.

Shear Wave

The eigenvalue

$$\lambda = u\kappa_x + v\kappa_y \tag{15c}$$

and right eigenvector

$$\tilde{\mathbf{R}}_2 = \left\{ \begin{array}{c} 0 \\ -c\kappa_y \\ c\kappa_x \\ 0 \end{array} \right\} \tag{15d}$$

represent a change in velocity direction, and can be thought of as a shear wave. The wave travels with the projected fluid velocity.

Entropy Wave

The same eigenvalue

$$\lambda = u\kappa_x + v\kappa_y \tag{15e}$$

and its other right eigenvector

$$\tilde{\mathbf{R}}_3 = \left\{ \begin{array}{c} \rho \\ 0 \\ 0 \\ 0 \end{array} \right\} \tag{15f}$$

represent an entropy wave. The wave travels with the projection of the fluid velocity onto the direction vector $\boldsymbol{\kappa}$, as above.

Second Acoustic Wave

The eigenvalue

$$\lambda = u\kappa_x + v\kappa_y + c \tag{15g}$$

and right eigenvector

$$\tilde{\mathbf{R}}_4 = \left\{ \begin{array}{c} \rho \\ c\kappa_x \\ c\kappa_y \\ \rho c^2 \end{array} \right\} \tag{15h}$$

represent an acoustic disturbance. The wave travels with the projected fluid velocity plus the speed of sound.

The "characteristic variables" for a given value of (κ_x,κ_y) may be computed, giving

$$d\mathrm{w} \;=\; \mathbf{R}^{-1}\delta\tilde{\mathrm{u}} \tag{16a}$$

$$= \left\{ \begin{array}{c} \frac{1}{2}\left[\frac{\delta p}{\rho c^2} - \left[\kappa_x \frac{\Delta u}{c} + \kappa_y \frac{\Delta v}{c}\right]\right] \\ \kappa_x \frac{\Delta v}{c} - \kappa_y \frac{\Delta u}{c} \\ \frac{\delta \rho}{\rho} - \frac{\delta p}{\rho c^2} \\ \frac{1}{2}\left[\frac{\delta p}{\rho c^2} + \left[\kappa_x \frac{\Delta u}{c} + \kappa_y \frac{\Delta v}{c}\right]\right] \end{array} \right\} . \tag{16b}$$

This, however, does not say anything about the choice of the direction vector $\boldsymbol{\kappa}=(\kappa_x,\kappa_y)$. Time-dependent and steady solutions of the Euler equations may include waves travelling in particular directions. It is the way in which the direction vectors for these waves are chosen that distinguishes the various wave-like models for the Euler equations.

Most modern schemes for the two-dimensional Euler equations are based on grid-contravariant directions. The conservative Euler equations (Equation 12a) are integrated over a cell $\Omega_{i,j}$, with boundary $\partial\Omega_{i,j}$. This gives

$$\iint_{\Omega_{i,j}} \frac{\partial \mathbf{U}}{\partial t} dA + \iint_{\Omega_{i,j}} \left(\frac{\partial \mathbf{F}}{\partial x} + \frac{\partial \mathbf{G}}{\partial y} \right) = 0 . \tag{17a}$$

The second integral is converted to a line integral over the cell boundary:

$$\iint_{\Omega_{i,j}} \frac{\partial \mathbf{U}}{\partial t} dA + \oint_{\partial\Omega_{i,j}} (\mathbf{F}dy - \mathbf{G}dx) = 0 . \tag{17b}$$

The first integral can be expressed in terms of the change in the average state $\bar{\mathbf{U}}$ in the cell, and the line integral becomes a sum over the faces (say, four) of the cell:

$$A\frac{d\bar{\mathbf{U}}}{dt} + \sum_{\ell=1}^{4} (\mathbf{F}\Delta y - \mathbf{G}\Delta x)_\ell = 0 . \tag{17c}$$

After introducing the cell-face length Δs,

$$\Delta s^2 = \Delta x^2 + \Delta y^2, \tag{17d}$$

Equation 17c can be written as

$$A\frac{d\bar{\mathbf{U}}}{dt} + \sum_{\ell=1}^{4} \mathbf{F}_n^{(\ell)} \Delta s_\ell = 0 , \tag{17e}$$

where $\mathbf{F}_n$ is the flux normal to the cell face

$$\mathbf{F}_n = \left\{ \begin{array}{c} \rho u_\perp \\ \rho u_\perp u + p\cos\theta_g \\ \rho u_\perp v - p\sin\theta_g \\ \rho u_\perp h_0 \end{array} \right\} ; \tag{17f}$$

$$\cos\theta_g = \Delta y/\Delta s\,, \tag{17g}$$

$$\sin\theta_g = -\Delta x/\Delta s\,, \tag{17h}$$

$$u_\perp = u\cos\theta_g - v\sin\theta_g\,, \tag{17i}$$

$$u_\parallel = u\sin\theta_g + v\cos\theta_g\,. \tag{17j}$$

Roe's flux-difference splitting consists of writing the interface flux as

$$\mathbf{F}(\mathbf{U_L},\mathbf{U_R}) = \frac{1}{2}\left(\mathbf{F_L}+\mathbf{F_R}\right) - \frac{1}{2}\sum_{k=1}^{4}\left|\hat{\lambda}_k\right|\Delta V_k\hat{\mathbf{R}}_k\,, \tag{18}$$

where the eigenvectors are

$$\hat{\mathbf{R}}_1 = \begin{Bmatrix} 1 \\ \hat{u}-\hat{c}\cos\theta_g \\ \hat{v}-\hat{c}\sin\theta_g \\ \hat{h}_0-\hat{u}_\perp\hat{c} \end{Bmatrix}, \tag{19a}$$

$$\hat{\mathbf{R}}_2 = \begin{Bmatrix} 0 \\ -\sin\theta_g \\ \cos\theta_g \\ \hat{u}_\parallel \end{Bmatrix}, \tag{19b}$$

$$\hat{\mathbf{R}}_3 = \begin{Bmatrix} 1 \\ \hat{u} \\ \hat{v} \\ \frac{1}{2}(\hat{u}^2+\hat{v}^2) \end{Bmatrix}, \tag{19c}$$

$$\hat{\mathbf{R}}_4 = \begin{Bmatrix} 1 \\ \hat{u}+\hat{c}\cos\theta_g \\ \hat{v}+\hat{c}\sin\theta_g \\ \hat{h}_0+\hat{u}_\perp\hat{c} \end{Bmatrix}; \tag{19d}$$

$\Delta\mathbf{V}$ is given by

$$\Delta\mathbf{V} = \begin{Bmatrix} \frac{1}{2\hat{c}^2}\left(\Delta p - \hat{\rho}\hat{c}\Delta u_\perp\right) \\ \hat{\rho}\Delta u_\parallel \\ -\frac{1}{\hat{c}^2}\left(\Delta p - \hat{c}^2\Delta\rho\right) \\ \frac{1}{2\hat{c}^2}\left(\Delta p + \hat{\rho}\hat{c}\Delta u_\perp\right\} \end{Bmatrix}; \tag{20}$$

and the wave speeds are

$$\lambda_1 = \hat{u}_\perp - \hat{c}, \tag{21a}$$

$$\lambda_2 = \hat{u}_\perp, \tag{21b}$$

$$\lambda_3 = \hat{u}_\perp, \tag{21c}$$

$$\lambda_4 = \hat{u}_\perp + \hat{c}. \tag{21d}$$

For the two-dimensional case,

$$\hat{v} = v_L w + v_R(1-w), \tag{22a}$$

$$\hat{c} = \sqrt{(\gamma-1)\left[\hat{h}_0 - \frac{1}{2}(\hat{u}^2+\hat{v}^2)\right]}, \tag{22b}$$

and $\hat{\rho}$, $\hat{v}$ and $\hat{h}_0$ are as before.

2.3 Wave Models for the 2D Euler Equations

For a more general two-dimensional scheme, directions other than the grid-contravariant directions should be chosen. The direction vector $\boldsymbol{\kappa}$ can not be determined directly from the equations of motion, however. In general, in multi-dimensional flow, information may propagate in an infinite number of directions. Thus a dominant direction, or directions, must be chosen for a discrete wave model, based on local flow values.

There are basically two approaches to determining the propagation directions:

1. an *ad hoc* choice of a dominant direction, or directions, based on physical considerations;

2. using local flow gradients to "fit" a set of discrete waves to the residual, solving for the appropriate convection directions.

The first approach is by far the simpler of the two. In it, dominant directions are chosen, and the residual is interpreted as a sum of waves moving in these directions. This approach is actually the one used in most current flow solvers, with the dominant directions taken to be the grid contravariant directions. This is clearly not physical. If, for instance, a stationary normal shock were to lie oblique to the grid, the difference between the pre- and post-shock states would be interpreted as a combination of a compression and a shear, instead of just

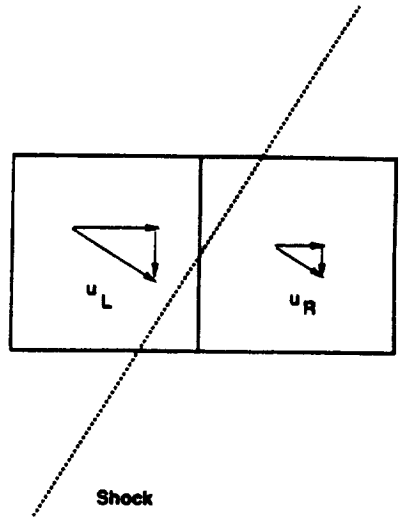

Figure 1: Representation of a Shock Oblique to the Grid

as a compression (See Figure 1). If, however, the shock were studied in a frame normal to it, there would be no element of shear seen in the difference between the two states (See Figure 2).

Clearly, then, the choice of dominant direction can have an effect on the solution. But what direction should be chosen? In the previous example, choosing the flow direction would have given the proper behavior, since the shock was normal to the flow direction. This would not be true for an oblique shock, however. For a non-curved oblique shock, directions that would give the proper behavior include:

- the pressure gradient direction;
- the density gradient direction;
- the entropy gradient direction.

Another direction of interest is the velocity difference direction,

$$\kappa_x = \frac{u_R - u_L}{\sqrt{(u_R - u_L)^2 + (v_R - v_L)^2}} \tag{23a}$$

$$\kappa_y = \frac{v_R - v_L}{\sqrt{(u_R - u_L)^2 + (v_R - v_L)^2}} \tag{23b}$$

In this direction, the difference in the two states ($\tilde{\mathbf{U}}_\mathbf{R}$, $\tilde{\mathbf{U}}_\mathbf{L}$) may be interpreted (based on the velocities) as *either* a shock aligned normal to the velocity difference direction, *or* a shear aligned parallel to the velocity difference direction (See Figure 2). Not until the difference in pressure between the two states is taken into account can it be determined whether a shock (large pressure difference) or a shear (zero or small pressure change) exists.

The second approach is more intricate, and has led thus far to two methods of calculating propagation directions. The first method is based on decomposition of local gradients, and is due to Roe [3]. The second method is based on an approximate diagonalization of the Euler equations, and is due to Hirsch *et al* [4] and Deconinck *et al* [5].

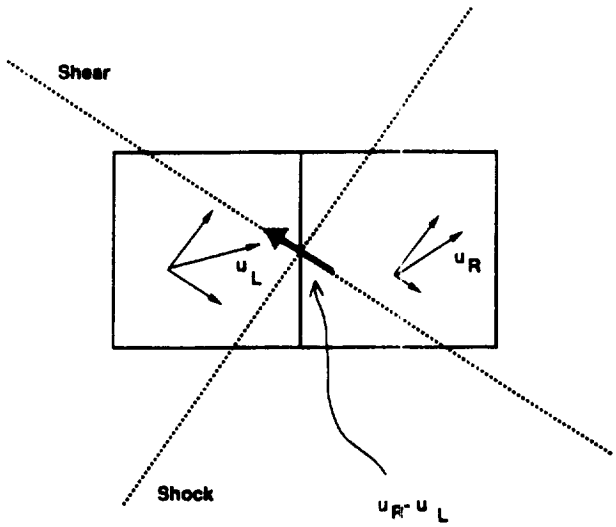

Figure 2: Velocity Difference Direction

In the first method, an *a priori* model for the number and type of waves is made, and then angles, strengths and speeds of the waves are determined from local data. The example carried out here will consisit of four acoustic waves, a shear wave and an entropy wave. The acoustic waves are taken to have unknown strengths α_1, α_2, α_3 and α_4, and orientations θ, $\theta+\pi/2$, $\theta+\pi$, and $\theta+3\pi/2$, respectively. The entropy wave is taken to have strength β, and orientation ϕ. The shear is represented by a uniform vorticity ω (See Figure 3). This model gives eight unknowns (α_1, α_2, α_3, α_4,β, ω, θ, ϕ). The eight equations come from expressing the components of the local gradients of density, velocities and pressure in terms of these waves. The entropy wave, for example, contributes

$$\beta\tilde{\mathbf{R}}_1\left(\cos\phi\hat{\mathbf{e}}_\mathbf{x}+\sin\phi\hat{\mathbf{e}}_\mathbf{y}\right) \tag{24a}$$

to the local gradient $\nabla\tilde{\mathbf{U}}$. The first acoustic wave contributes

$$\alpha_1\tilde{\mathbf{R}}_3\left(\cos\theta\hat{\mathbf{e}}_\mathbf{x}+\sin\theta\hat{\mathbf{e}}_\mathbf{y}\right) \tag{24b}$$

where

$$\begin{aligned}\kappa_x &= \cos\theta\,,\\ \kappa_y &= \sin\theta\,.\end{aligned}$$

The other acoustic-wave contributions are calculated similarly. The contribution of the vorticity is

$$\left\{\begin{array}{c}0\\ -\frac{1}{2}\omega\hat{\mathbf{e}}_\mathbf{y}\\ \frac{1}{2}\omega\hat{\mathbf{e}}_\mathbf{x}\\ 0\end{array}\right\}. \tag{24c}$$

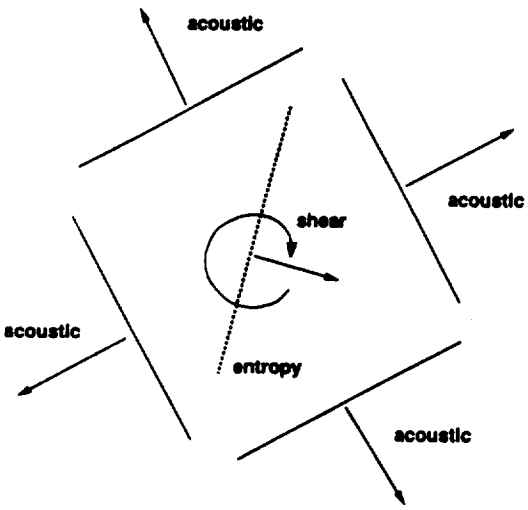

Figure 3: Roe's Wave Decomposition

Summing the contributions of these waves gives the system of equations

$$\alpha_1 \cos\theta + \alpha_2 \cos\theta - \alpha_3 \sin\theta - \alpha_4 \sin\theta = \frac{1}{\rho c^2}\frac{\partial p}{\partial x} \quad (25a)$$

$$\alpha_1 \sin\theta + \alpha_2 \sin\theta - \alpha_3 \cos\theta - \alpha_4 \cos\theta = \frac{1}{\rho c^2}\frac{\partial p}{\partial y} \quad (25b)$$

$$\alpha_1 \cos^2\theta - \alpha_2 \cos^2\theta + \alpha_3 \sin^2\theta - \alpha_4 \sin^2\theta = \frac{1}{c}\frac{\partial u}{\partial x} \quad (25c)$$

$$\alpha_1 \sin\theta\cos\theta - \alpha_2 \sin\theta\cos\theta - \alpha_3 \sin\theta\cos\theta + \alpha_4 \sin\theta\cos\theta - \frac{\omega}{2c} = \frac{1}{c}\frac{\partial u}{\partial y} \quad (25d)$$

$$\alpha_1 \sin\theta\cos\theta - \alpha_2 \sin\theta\cos\theta - \alpha_3 \sin\theta\cos\theta + \alpha_4 \sin\theta\cos\theta + \frac{\omega}{2c} = \frac{1}{c}\frac{\partial v}{\partial x} \quad (25e)$$

$$\alpha_1 \sin^2\theta - \alpha_2 \sin^2\theta + \alpha_3 \cos^2\theta - \alpha_4 \cos^2\theta = \frac{1}{c}\frac{\partial v}{\partial y} \quad (25f)$$

$$\alpha_1 \cos\theta + \alpha_2 \cos\theta - \alpha_3 \sin\theta - \alpha_4 \sin\theta + \beta\cos\phi = \frac{1}{\rho}\frac{\partial \rho}{\partial x} \quad (25g)$$

$$\alpha_1 \sin\theta + \alpha_2 \sin\theta + \alpha_3 \cos\theta + \alpha_4 \cos\theta + \beta\cos\phi = \frac{1}{\rho}\frac{\partial \rho}{\partial y} \quad (25h)$$

This system can be solved for the strengths and angles of the waves, giving

$$\omega = \left(\frac{\partial v}{\partial x} - \frac{\partial u}{\partial y}\right) \quad (26a)$$

$$\beta\cos\phi = \frac{1}{\rho}\left(\frac{\partial \rho}{\partial x} - \frac{1}{c^2}\frac{\partial p}{\partial x}\right) \quad (26b)$$

$$\beta\sin\phi = \frac{1}{\rho}\left(\frac{\partial \rho}{\partial y} - \frac{1}{c^2}\frac{\partial p}{\partial y}\right) \quad (26c)$$

$$\tan 2\theta = \frac{\left(\frac{\partial v}{\partial x} + \frac{\partial u}{\partial y}\right)}{\left(\frac{\partial u}{\partial x} - \frac{\partial v}{\partial y}\right)} \tag{26d}$$

$$\alpha_1 - \alpha_2 = \frac{1}{2c}\left[\frac{\partial u}{\partial x} + \frac{\partial v}{\partial y} + \sqrt{\left(\frac{\partial v}{\partial x} + \frac{\partial u}{\partial y}\right)^2 + \left(\frac{\partial u}{\partial x} - \frac{\partial v}{\partial y}\right)^2}\right] \tag{26e}$$

$$\alpha_3 - \alpha_4 = \frac{1}{2c}\left[\frac{\partial u}{\partial x} + \frac{\partial v}{\partial y} - \sqrt{\left(\frac{\partial v}{\partial x} + \frac{\partial u}{\partial y}\right)^2 + \left(\frac{\partial u}{\partial x} - \frac{\partial v}{\partial y}\right)^2}\right] \tag{26f}$$

$$\alpha_1 + \alpha_2 = \frac{1}{\rho c^2}\left(\frac{\partial p}{\partial x}\cos\theta + \frac{\partial p}{\partial y}\sin\theta\right) \tag{26g}$$

$$\alpha_3 + \alpha_4 = \frac{1}{\rho c^2}\left(\frac{\partial p}{\partial y}\cos\theta - \frac{\partial p}{\partial x}\sin\theta\right) . \tag{26h}$$

Thus a scheme based on this model would, at each iteration, calculate the derviatives $\nabla\tilde{\mathbf{U}}$, and use the above formulas to solve for the unknowns α_1, α_2, α_3, α_4,β, ω, θ, and ϕ. Practical schemes based on this composition have yet to be developed, but work towards this end has been done by Roe [3], Deconinck [6] and Kröner [7]. This is an eight-wave model, decomposing the difference between two states into eight separate waves. The flux in a standard grid-aligned Roe scheme is based on a four wave model.

In the second method, an approximate diagonalization of the Euler equations is sought. It is of the form

$$\frac{\partial \mathbf{W}^*}{\partial t} + \mathbf{D_x}\frac{\partial \mathbf{W}^*}{\partial x} + \mathbf{D_y}\frac{\partial \mathbf{W}^*}{\partial y} = \mathbf{S}\,, \tag{27a}$$

where $\mathbf{W}^*$ is a vector of convected quantities (entropy, a component of velocity, and two acoustic-like variables), $\mathbf{D_x}$ and $\mathbf{D_y}$ are diagonal matrices of convection speeds, and $\mathbf{S}$ is a source term. In this approach, two $\boldsymbol{\kappa}$-vectors are chosen in such a way as to minimize the components of the source term $\mathbf{S}$. They are $\boldsymbol{\kappa}^{(1)}$ for the velocity-component convection and $\boldsymbol{\kappa}^{(2)}$ for the acoustic-like convection. With the two $\boldsymbol{\kappa}$ vectors,

$$d\mathbf{W}^* = \left\{ \begin{array}{c} -\boldsymbol{\kappa}^{(2)} \cdot \Delta\mathbf{u} - \frac{\Delta p}{\rho c} \\ \kappa_y^{(1)}\Delta u - \kappa_x^{(1)}\Delta v \\ \Delta\rho - \frac{\Delta p}{c^2} \\ \boldsymbol{\kappa}^{(2)} \cdot \Delta\mathbf{u} - \frac{\Delta p}{\rho c} \end{array} \right\} ; \tag{27b}$$

$$\mathbf{D_x} = \begin{bmatrix} u - \kappa_y^{(2)} c & 0 & 0 & 0 \\ 0 & u & 0 & 0 \\ 0 & 0 & u & 0 \\ 0 & 0 & 0 & u + \kappa_y^{(2)} c \end{bmatrix}, \tag{27c}$$

$$\mathbf{D_y} = \begin{bmatrix} v - \kappa_y^{(2)} c & 0 & 0 & 0 \\ 0 & v & 0 & 0 \\ 0 & 0 & v & 0 \\ 0 & 0 & 0 & v + \kappa_y^{(2)} c \end{bmatrix}; \tag{27d}$$

$$\mathbf{S} = \begin{Bmatrix} -c\left(\kappa_y^{(2)} \frac{\partial}{\partial x} - \kappa_x^{(2)} \frac{\partial}{\partial y}\right) W_2^* \\ -\frac{c}{2}\left(\kappa_y^{(1)} \frac{\partial}{\partial x} - \kappa_x^{(1)} \frac{\partial}{\partial y}\right)\left(W_1^* + W_4^*\right) \\ 0 \\ -c\left(\kappa_y^{(2)} \frac{\partial}{\partial x} - \kappa_x^{(2)} \frac{\partial}{\partial y}\right) W_2^* \end{Bmatrix}. \tag{27e}$$

The right eigenvector matrix $\mathbf{P}^*$ for the transformation

$$d\mathbf{W}^* = \mathbf{P}^* d\mathbf{U} \tag{28}$$

is given, in columns, by

$$\mathbf{P}^{*(1)} = \begin{bmatrix} \frac{\rho}{2c} \\ \frac{\rho}{2c\boldsymbol{\kappa}^{(1)} \cdot \boldsymbol{\kappa}^{(2)}}\left(u\boldsymbol{\kappa}^{(1)} \cdot \boldsymbol{\kappa}^{(2)} - c\kappa_x^{(1)}\right) \\ \frac{\rho}{2c\boldsymbol{\kappa}^{(1)} \cdot \boldsymbol{\kappa}^{(2)}}\left(v\boldsymbol{\kappa}^{(1)} \cdot \boldsymbol{\kappa}^{(2)} - c\kappa_y^{(1)}\right) \\ \frac{\rho}{2c\boldsymbol{\kappa}^{(1)} \cdot \boldsymbol{\kappa}^{(2)}}\left(h_0\boldsymbol{\kappa}^{(1)} \cdot \boldsymbol{\kappa}^{(2)} - c\mathbf{u} \cdot \boldsymbol{\kappa}^{(1)}\right) \end{bmatrix}, \tag{29a}$$

$$\mathbf{P}^{*(2)} = \begin{bmatrix} 0 \\ \frac{\rho\kappa_y^{(2)}}{\boldsymbol{\kappa}^{(1)} \cdot \boldsymbol{\kappa}^{(2)}} \\ -\frac{\rho\kappa_x^{(2)}}{\boldsymbol{\kappa}^{(1)} \cdot \boldsymbol{\kappa}^{(2)}} \\ \frac{\rho u\kappa_y^{(2)} - \rho v\kappa_x^{(2)}}{\boldsymbol{\kappa}^{(1)} \cdot \boldsymbol{\kappa}^{(2)}} \end{bmatrix}, \tag{29b}$$

$$\mathbf{P}^{*(3)} = \begin{bmatrix} 1 \\ u \\ v \\ \frac{u^2+v^2}{2} \end{bmatrix}, \tag{29c}$$

$$\mathbf{P}^{*(4)} = \begin{bmatrix} \frac{\rho}{2c} \\ \frac{\rho}{2c\boldsymbol{\kappa}^{(1)}\cdot\boldsymbol{\kappa}^{(2)}}\left(u\boldsymbol{\kappa}^{(1)}\cdot\boldsymbol{\kappa}^{(2)} + c\kappa_x^{(1)}\right) \\ \frac{\rho}{2c\boldsymbol{\kappa}^{(1)}\cdot\boldsymbol{\kappa}^{(2)}}\left(v\boldsymbol{\kappa}^{(1)}\cdot\boldsymbol{\kappa}^{(2)} + c\kappa_y^{(1)}\right) \\ \frac{\rho}{2c\boldsymbol{\kappa}^{(1)}\cdot\boldsymbol{\kappa}^{(2)}}\left(h_0\boldsymbol{\kappa}^{(1)}\cdot\boldsymbol{\kappa}^{(2)} + c\mathbf{u}\cdot\boldsymbol{\kappa}^{(1)}\right) \end{bmatrix}. \tag{29d}$$

These equations are general, holding for any choices of $\boldsymbol{\kappa}^{(1)}$ and $\boldsymbol{\kappa}^{(2)}$. Hirsch *et al* [4] show that, in order to minimize the source terms, one needs a $\boldsymbol{\kappa}^{(1)}$ that is aligned locally with the pressure gradient, and a $\boldsymbol{\kappa}^{(2)}$ that is related to the strain-rate tensor. That is, $\boldsymbol{\kappa}^{(1)}$ is given by

$$\boldsymbol{\kappa}^{(1)} = \frac{\nabla p}{|\nabla p|} \tag{30a}$$

and $\boldsymbol{\kappa}^{(2)}$ is computed from the velocity derivatives in the following way: if

$$\left(\frac{\partial v}{\partial x} + \frac{\partial u}{\partial y}\right)^2 - 4\frac{\partial u}{\partial x}\frac{\partial v}{\partial y} \leq 0 \tag{30b}$$

then the propagation angle

$$\tan\theta = \frac{\frac{\partial v}{\partial x} + \frac{\partial u}{\partial y}}{2\frac{\partial u}{\partial x}} \tag{30c}$$

is calculated; otherwise, the possible propagation angles are given by

$$\tan\theta = \frac{\left(\frac{\partial v}{\partial x} + \frac{\partial u}{\partial y}\right) \pm \sqrt{\left(\frac{\partial v}{\partial x} + \frac{\partial u}{\partial y}\right)^2 - 4\frac{\partial u}{\partial x}\frac{\partial v}{\partial y}}}{2\frac{\partial u}{\partial x}}. \tag{30d}$$

The value of $\boldsymbol{\kappa}^{(2)}$ is then

$$\boldsymbol{\kappa}^{(2)} = \cos\theta\hat{\mathbf{e}}_\mathbf{x} + \sin\theta\hat{\mathbf{e}}_\mathbf{y}. \tag{30e}$$

The proper branch for Equation 30d is the one that maximizes the inner product $\boldsymbol{\kappa}^{(1)}\cdot\boldsymbol{\kappa}^{(2)}$.

This decomposition, as the standard grid-aligned Roe scheme, decomposes the residual using a four-wave model.

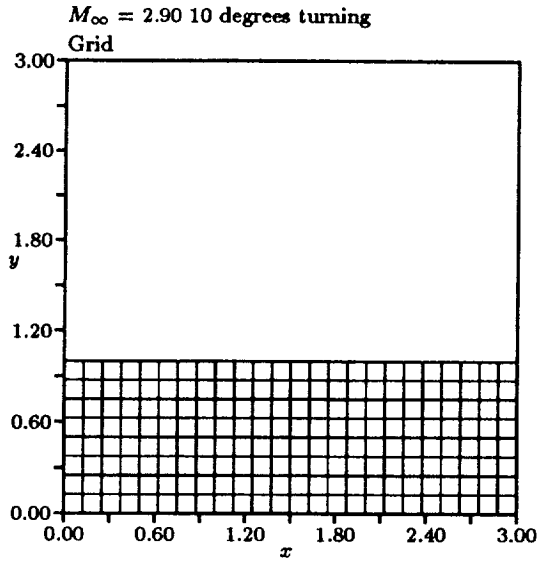

Figure 4: 24 × 8 Grid

2.4 Test Case for Multi-Dimensional Schemes

Three different schemes based on the above two-dimensional concepts are outlined in the following sections. The first is a scheme based on a downwind distribution. This scheme follows from ideas of Roe [3], and has been derived and implemented by Powell and Van Leer [8]. Schemes based on similar ideas have been developed by Struijs and Deconinck [9], Hirsch and Lacor [10] and Giles *et al* [11]. The second is a scheme based on a rotated Riemann solver. This idea, which is an extension of Jameson's work for potential flow [12], was first put forward by Davis [13], and has been further studied by Levy *et al* [14]. The third scheme is based on a generalized Riemann solver. The results of the three schemes are compared to those of a standard "grid-aligned" scheme based on Roe's approximate Riemann solver. The test-case is a reflected shock problem; an incoming Mach number of 2.9 with a turning of 10° in a 3×1 channel. The case was run on two grids: a 24×8 grid and a 96×32 grid. The grids on which the cases were run, and the baseline results for first- and second-order grid-aligned schemes are shown in Figures 4–13. All cases were run without flux-limiting. In Sections 3–5, the three methods tested are discussed in detail.

3 A Scheme Based on Downwind Distribution

3.1 A Scheme for the 2D Convection Equation

The heart of the first method, a downwind distribution scheme for the Euler equations, is a cell-vertex scheme for the two-dimensional convection equation

$$\frac{\partial u}{\partial t} + c_x \frac{\partial u}{\partial x} + c_y \frac{\partial u}{\partial y} = 0 \,. \tag{31}$$

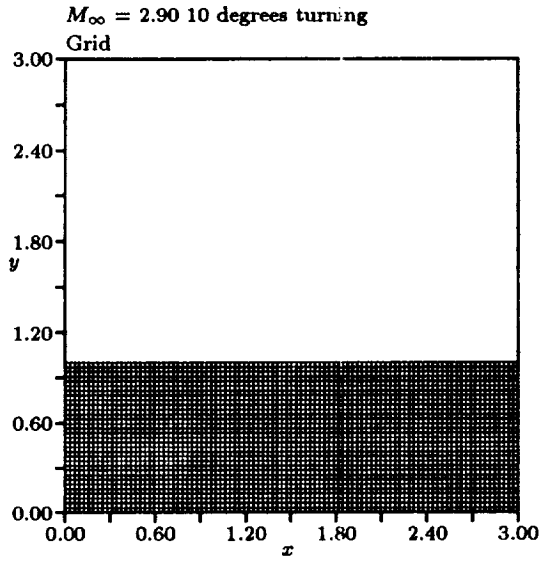

Figure 5: 96 × 32 Grid

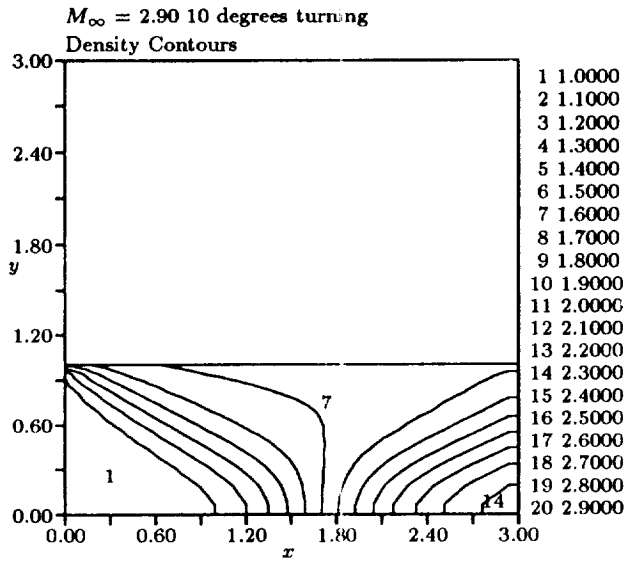

Figure 6: First-order Grid-Aligned Scheme — 24 × 8 Grid

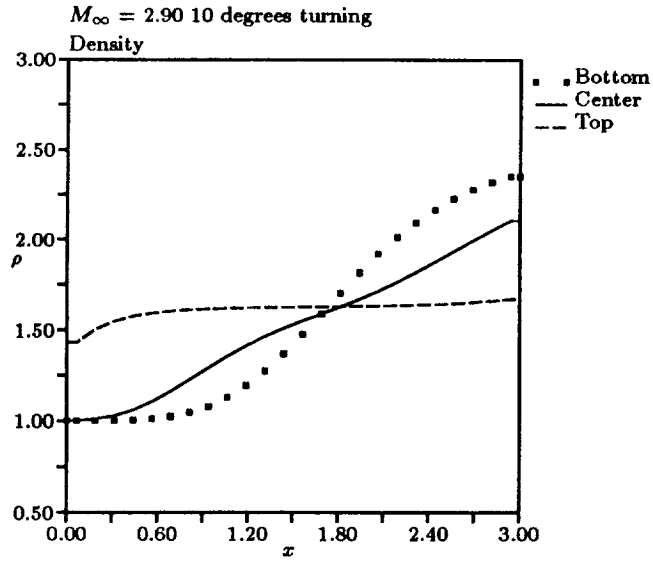

Figure 7: First-order Grid-Aligned Scheme — 24 × 8 Grid

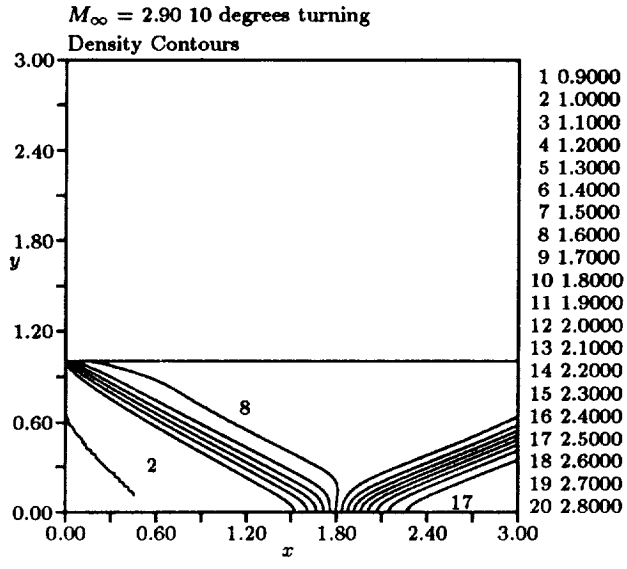

Figure 8: First-order Grid-Aligned Scheme — 96 × 32 Grid

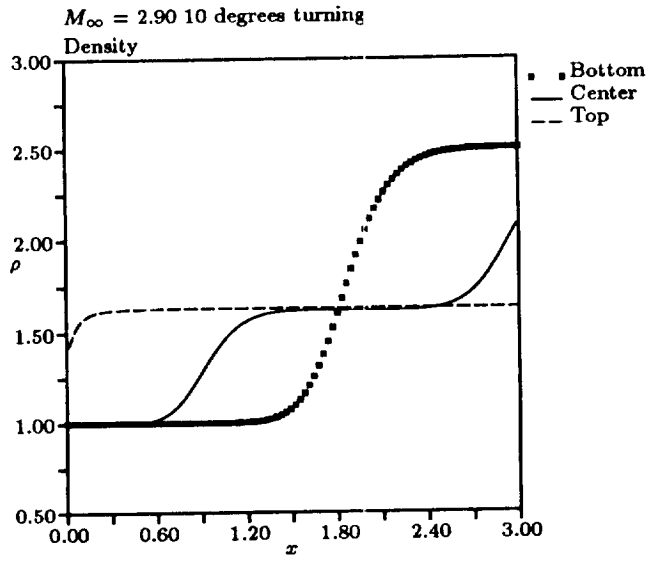

Figure 9: First-order Grid-Aligned Scheme — 96 × 32 Grid

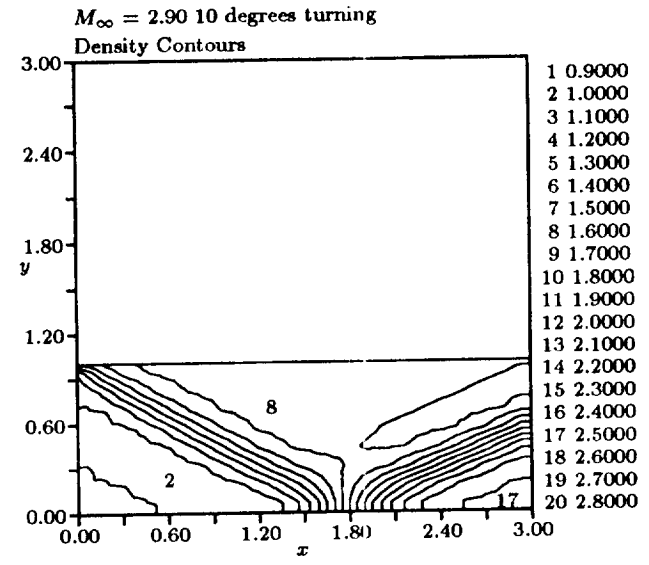

Figure 10: Second-order Grid-Aligned Scheme — 24 × 8 Grid

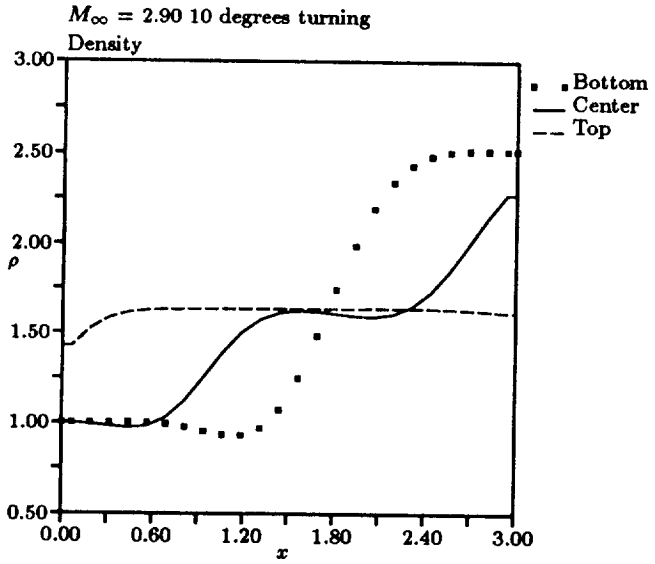

Figure 11: Second-order Grid-Aligned Scheme — 24 × 8 Grid

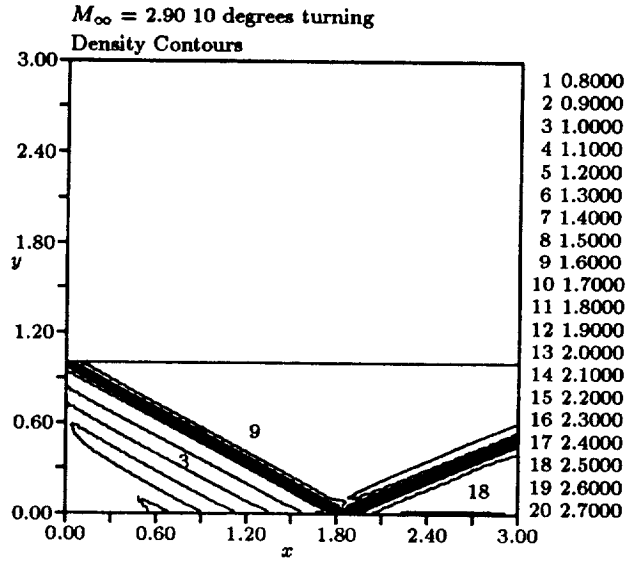

Figure 12: Second-order Grid-Aligned Scheme — 96 × 32 Grid

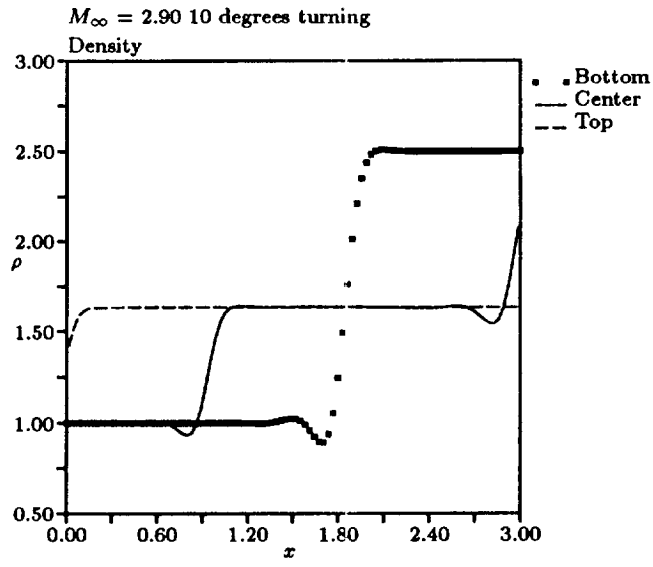

Figure 13: Second-order Grid-Aligned Scheme — 96 × 32 Grid

This scheme is analyzed below. On a uniform Cartesian grid, the residual for the convection equation is given by

$$Res_{i+\frac{1}{2},j+\frac{1}{2}} = \frac{\partial u}{\partial t} \tag{32a}$$

$$= -\frac{c_x}{\Delta x}\left(u_{i+1,j+\frac{1}{2}} - u_{i,j+\frac{1}{2}}\right) - \frac{c_y}{\Delta y}\left(u_{i+\frac{1}{2},j+1} - u_{i+\frac{1}{2},j}\right), \tag{32b}$$

where the semi-integer index denotes a average over a cell-face, i.e.

$$u_{i+\frac{1}{2},j} = \frac{1}{\Delta x}\int_{x_{i,j}}^{x_{i+1,j}} u\,dx\,, \tag{32c}$$

$$u_{i,j+\frac{1}{2}} = \frac{1}{\Delta y}\int_{y_{i,j}}^{y_{i,j+1}} u\,dy\,. \tag{32d}$$

These cell-face averages may be approximated using trapezoidal integration, giving the second-order approximation

$$u_{i+\frac{1}{2},j} = \frac{u_{i,j} + u_{i+1,j}}{2}, \tag{32e}$$

$$u_{i,j+\frac{1}{2}} = \frac{u_{i,j} + u_{i,j+1}}{2}. \tag{32f}$$

Using these formulas for the cell-face averages, the Fourier footprint of the flux integration for a cell is

$$\mathcal{F}(\Delta t Res) = -2i\left[\nu_x \sin\frac{\beta_x}{2}\cos\frac{\beta_y}{2} + \nu_y \sin\frac{\beta_y}{2}\cos\frac{\beta_x}{2}\right], \tag{33a}$$

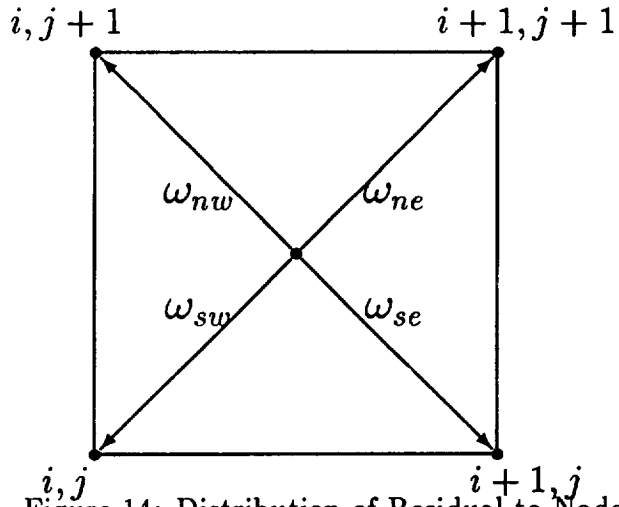

Figure 14: Distribution of Residual to Nodes

where the β's are the Fourier variables and the ν's are the Courant numbers

$$\nu_x = \frac{c_x \Delta t}{\Delta x} \tag{33b}$$

$$\nu_y = \frac{c_y \Delta t}{\Delta y}. \tag{33c}$$

To update the nodes, the cell-centered residual, given in Equation 32b, multiplied by Δt, will be sent to the nodes (i,j), $(i+1,j)$, $(i+1,j+1)$ and $(i,j+1)$ with weights ω_{sw}, ω_{se}, ω_{ne}, and ω_{nw} respectively (see Figure 14). The Fourier footprint of this distribution step is given by

$$\begin{aligned} \mathcal{F}(Dist) &= \left[(\omega_{ne} + \omega_{sw}) \cos \frac{\beta_x + \beta_y}{2} + (\omega_{nw} + \omega_{se}) \cos \frac{\beta_x - \beta_y}{2}\right] \\ &\quad + i \left[(\omega_{sw} - \omega_{ne}) \sin \frac{\beta_x + \beta_y}{2} + (\omega_{nw} - \omega_{se}) \sin \frac{\beta_x - \beta_y}{2}\right]. \end{aligned} \tag{33d}$$

If a simple forward-Euler time-stepping scheme is used, the net amplification factor for the entire scheme is

$$G(\nu_x, \nu_y, \beta_x, \beta_y) = 1 + \mathcal{F}(\Delta t Res)\, \mathcal{F}(Dist) \tag{33e}$$

The appropriate values for the ω's remain to be determined from the stability analysis. Since they correspond to convection directions, they should be determined by enforcing stability for the long waves (β_x,$\beta_y \to 0$).

Taking the limit of Equation 33e as $\beta_x, \beta_y \to 0$ yields the constraint

$$k^2 (\nu_x \beta_x + \nu_y \beta_y) = (\omega_{sw} - \omega_{ne}) \frac{\beta_x + \beta_y}{2} + (\omega_{nw} - \omega_{se}) \frac{\beta_x - \beta_y}{2}, \tag{34a}$$

where k is some real constant. An added constraint (conservation) is that the entire residual must be distributed,

$$\omega_{ne} + \omega_{sw} + \omega_{nw} + \omega_{se} = 1 . \tag{34b}$$

Also, by symmetry, if the ν_x and ν_y are such that convection is directly towards one node, all of the residual is distributed to that node, i.e.

$$\omega_{ne} = 1 \quad \text{if} \quad \nu_x = \nu_y > 0 ; \tag{34c}$$

$$\omega_{sw} = 1 \quad \text{if} \quad \nu_x = \nu_y < 0 ; \tag{34d}$$

$$\omega_{nw} = 1 \quad \text{if} \quad -\nu_x = \nu_y > 0 ; \tag{34e}$$

$$\omega_{se} = 1 \quad \text{if} \quad -\nu_x = \nu_y < 0 . \tag{34f}$$

Combining these conditions gives the distribution coefficients

$$\omega_{ne} = \max\left(0, \frac{(\nu_x + \nu_y)}{|\nu_x + \nu_y| + |\nu_x - \nu_y|}\right) \tag{35a}$$

$$\omega_{sw} = \max\left(0, \frac{-(\nu_x + \nu_y)}{|\nu_x + \nu_y| + |\nu_x - \nu_y|}\right) \tag{35b}$$

$$\omega_{nw} = \max\left(0, \frac{-(\nu_x - \nu_y)}{|\nu_x + \nu_y| + |\nu_x - \nu_y|}\right) \tag{35c}$$

$$\omega_{se} = \max\left(0, \frac{(\nu_x - \nu_y)}{|\nu_x + \nu_y| + |\nu_x - \nu_y|}\right) . \tag{35d}$$

These formulas state that the residual is sent only to the nodes that define the downwind face, and is distributed in a weighted manner between the two nodes on that face. For a plane wave moving in one of the coordinate directions, the two downwind weights are equal, and the scheme reduces to the standard one-dimensional upwind scheme. The stability constraint of the scheme is

$$\nu_x^2 + \nu_y^2 \leq 1 . \tag{36}$$

The locus of the scheme (i.e. the Fourier footprint of $F(\Delta t Res)F(Dist)$) is shown for 0°, 20° and 45° convection in Figures 15–17. The plots are generated by varying β_x and β_y discretely, which leads to a mesh of points within the continuous footprint of the locus. The circular stability boundary of forward-Euler time-stepping is circumscribed about the loci for reference. The loci are very different from those of first-order upwind or central-difference schemes. It is the wave that is convected at 45° that is damped the best, while waves at 0° (or 90°) are not damped well. This can be seen clearly in the contours of the amplification factor for the scheme, shown in Figures 18–20.

Some numerical results for a convected Gaussian on a 32×32 grid are given in Figures 21–23. The convection directions are 0°, 20° and 45°. In each case the Gaussian propagates across the grid virtually undistorted. The onset of a zebra instability can be seen in the 0° case, as predicted in the stability analysis. The amplitude of oscillations in this case is very small (on the order of 10^{-4}). The convergence history for each of the cases is shown in

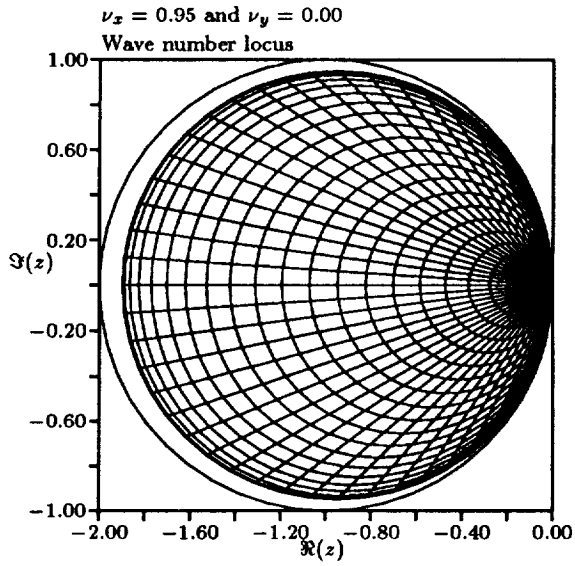

Figure 15: Fourier Footprint of Scheme — 0° wave

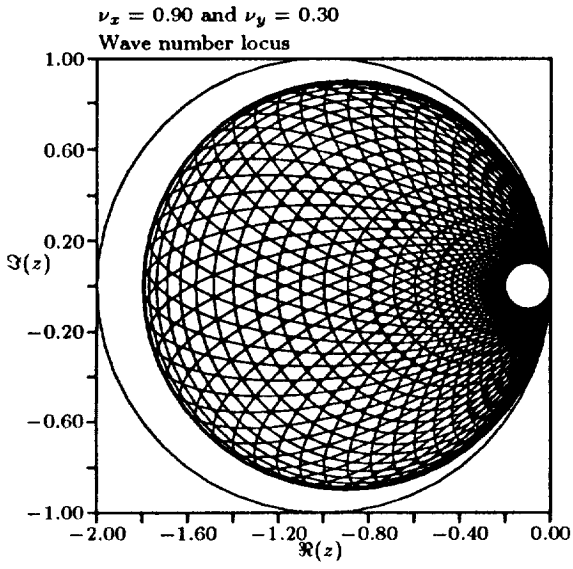

Figure 16: Fourier Footprint of Scheme — 20° wave

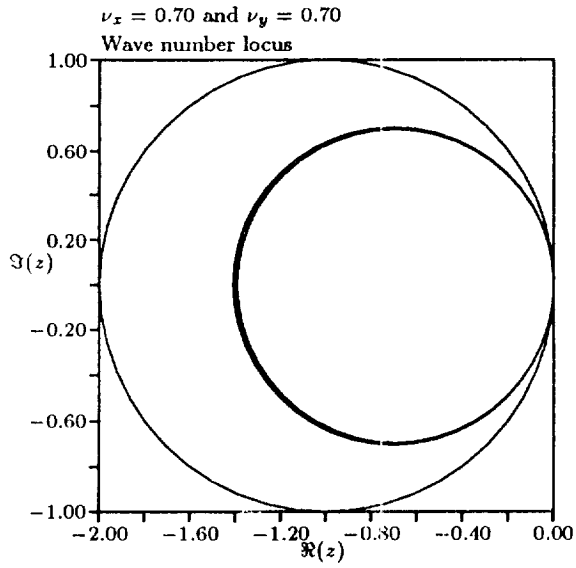

Figure 17: Fourier Footprint of Scheme — 45° wave

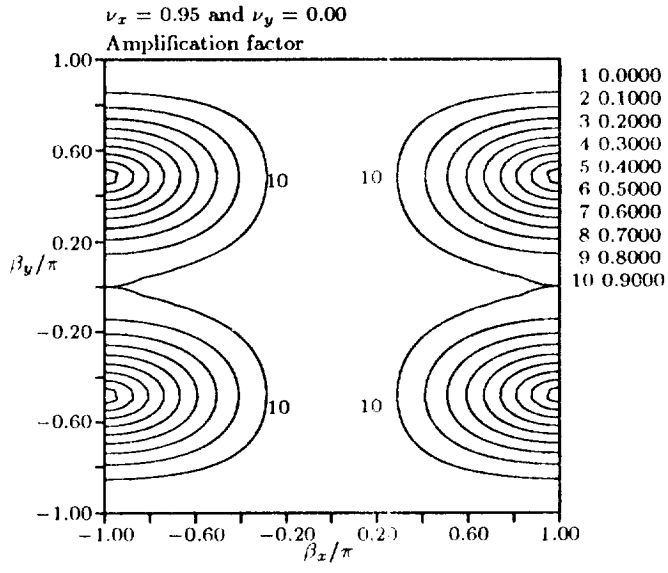

Figure 18: Amplification Factor of Scheme — 0° wave

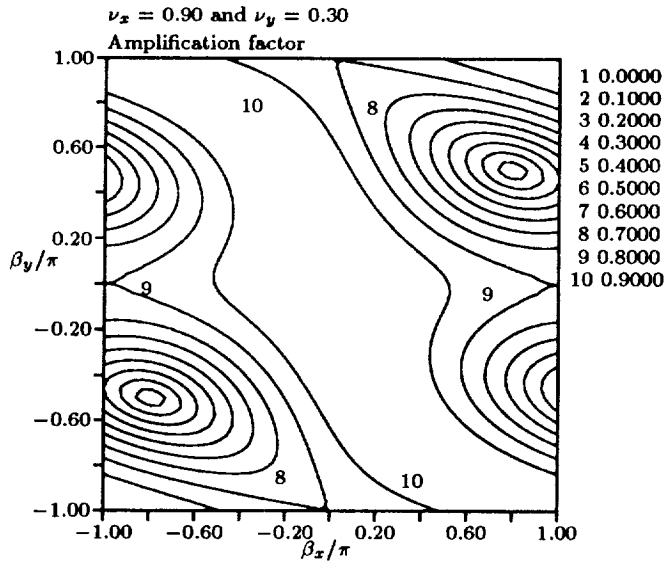

Figure 19: Amplification Factor of Scheme — 20° wave

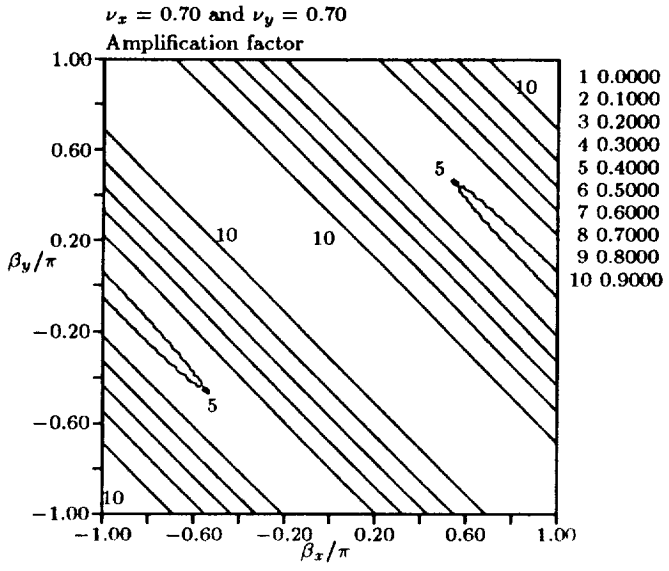

Figure 20: Amplification Factor of Scheme — 45° wave

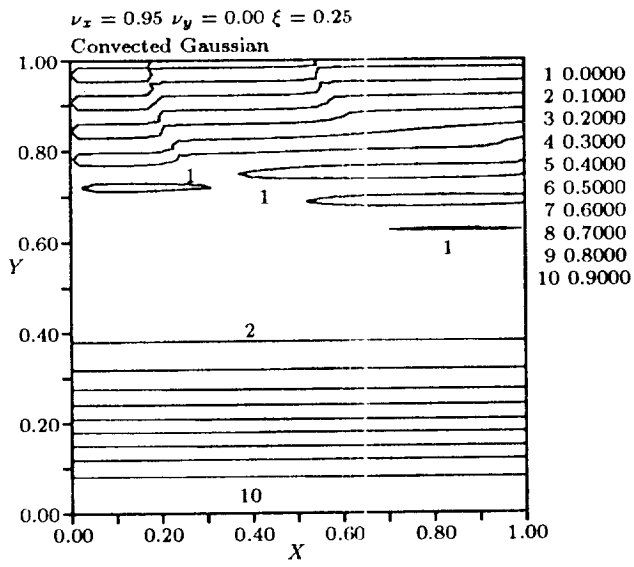

Figure 21: Gaussian Convected at 0°

Figures 24–26. The Gaussian convects at almost one cell per iteration, so that the slope of the residual curve changes drastically after approximately forty iterations. The 45° case, which has the best high-frequency damping, converges very quickly, while the 0° case converges very slowly.

The convergence characteristics of this scheme can be changed by an interesting variation in the way in which the downwind distribution step is implemented. In the above scheme, the residual for a cell was calculated, and split into contributions for each node of the cell. That is, a fraction ω_{ne} was distributed to the northeast node, a fraction ω_{nw} to the northwest node, and so on. A variation of this is not to split the residual at all, but to distribute the entire residual to one node, using the ω's as probabilities. That is, the residual is distributed to the northeast node with probability ω_{ne}, to the northwest node with probability ω_{nw}, and so on. This scheme gives the same steady-state solutions as the residual-splitting scheme, but the convergence characteristics of the 0° and 20° schemes are substantially different (Figures 27 and 28). The 45° case is not affected by the "random distribution" method.

Apparently the randomness of the distribution step helps kill high-frequency waves. However, in the early parts of the convergence history, this method can actually increase the residual (Figure 27). The best scheme is probably a hybrid of the residual-split method and the "random distribution" method.

3.2 Scheme for the Euler Equations

Just as in the scheme for the convection equation, the scheme for the Euler equations is made up of two primary steps:

1. a residual calculation based on a flux integral;

2. a residual distribution.

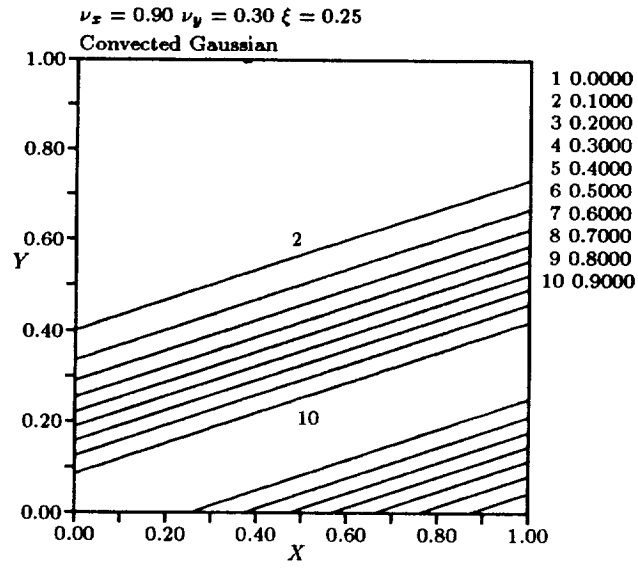

Figure 22: Gaussian Convected at 20°

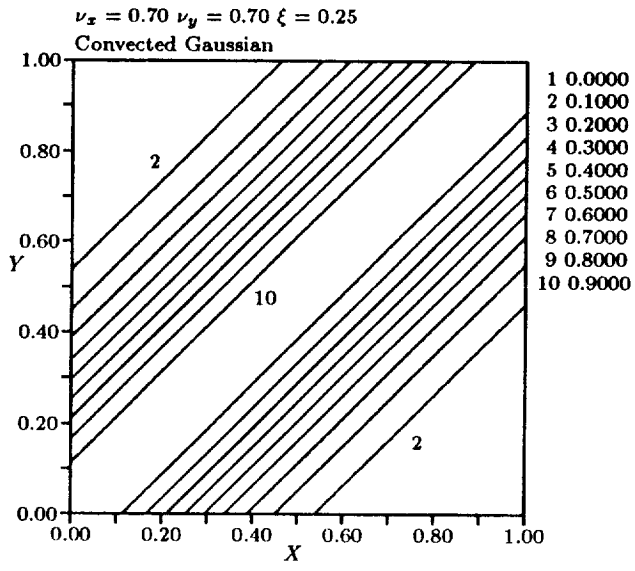

Figure 23: Gaussian Convected at 45°

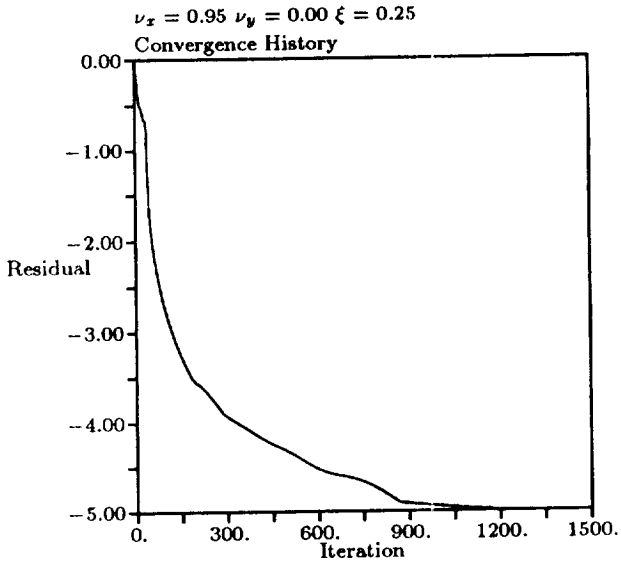

Figure 24: Convergence History for 0° Case

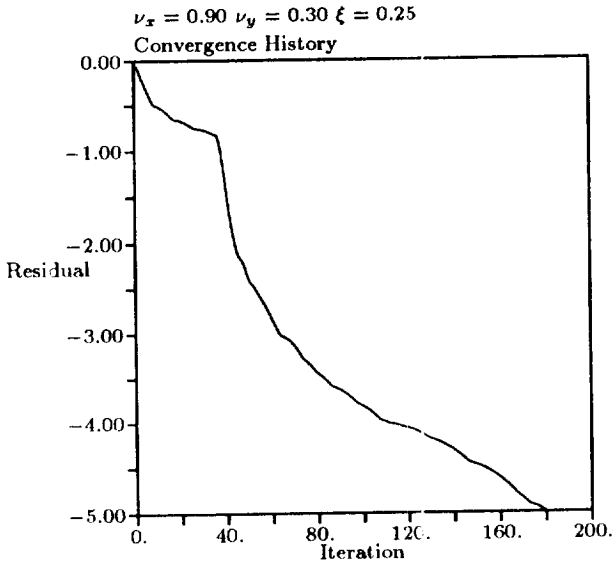

Figure 25: Convergence History for 20° Case

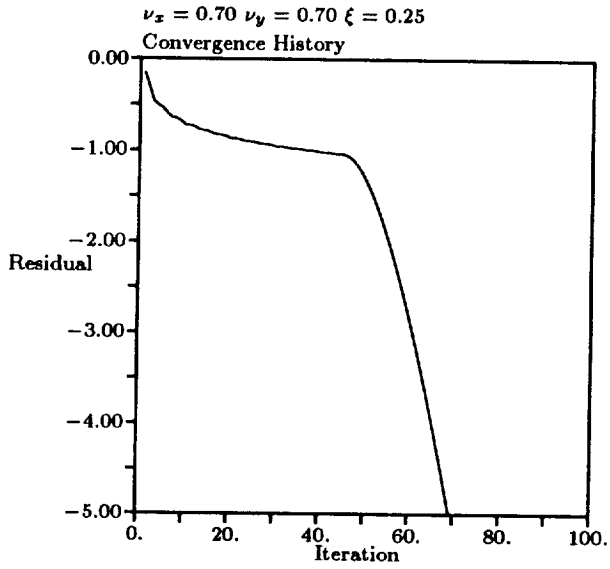

Figure 26: Convergence History for 45° Case

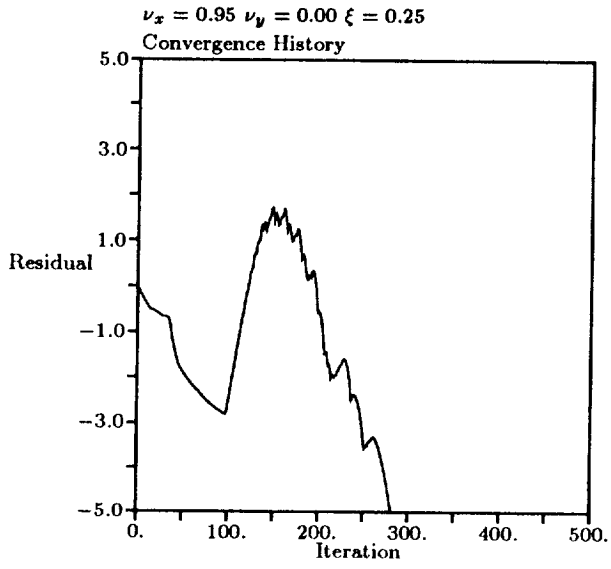

Figure 27: Convergence History for 0° "Random Distribution" Case

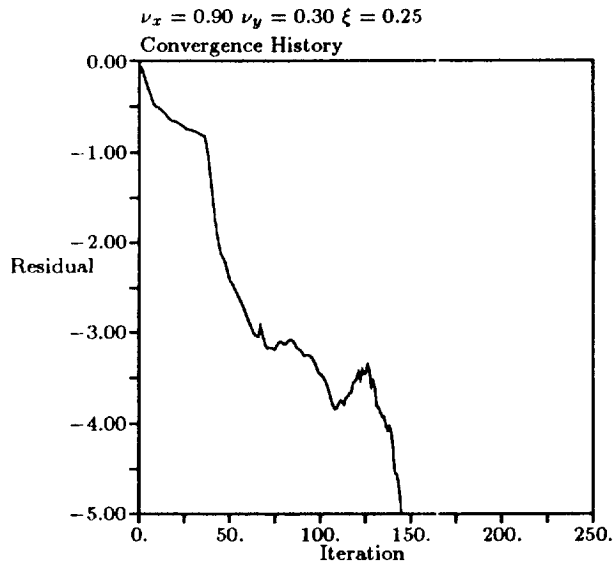

Figure 28: Convergence History for 20° "Random Distribution" Case

Each of these steps is somewhat more complicated for the system, however.

For the Euler equations, the residual for a cell is given by

$$\mathbf{Res}_{i+\frac{1}{2},j+\frac{1}{2}} = -\frac{1}{A}\oint_{\partial A}\left[\mathbf{F}\,dy - \mathbf{G}\,dx\right], \tag{37}$$

where A is the cell area and the integral is taken along the cell's boundary ∂A. The cells are now quadrilaterals, with faces lying along curvilinear coordinate lines $\xi = \xi_i$ and $\eta = \eta_j$. The boundary integral of Equation 37 is composed of contributions of fluxes normal to cell faces. To extend the approximation of Equations 32e and 32f so that they apply to the above residual, it is necessary to convert these to flux approximations. Equation 32f, for instance, when multiplied by $c_x\Delta y$, becomes an expression for the total flux across the cell-face centered at $(i, j+1/2)$:

$$c_x u_{i,j+\frac{1}{2}}\Delta y = \frac{c_x u_{i,j} + c_x u_{i,j+1}}{2}\Delta y\,. \tag{38}$$

With regard to the Euler equations, this translates directly into

$$\hat{\mathbf{F}}_{i,j+\frac{1}{2}}\Delta\eta = \frac{\mathbf{F}_{i,j} + \mathbf{F}_{i,j+1}}{2}\Delta_\eta y - \frac{\mathbf{G}_{i,j} + \mathbf{G}_{i,j+1}}{2}\Delta_\eta x\,, \tag{39a}$$

in which the following notation is used:

$$\Delta_\eta x = x_{i,j+1} - x_{i,j} \tag{39b}$$

$$\Delta_\eta y = y_{i,j+1} - y_{i,j} \tag{39c}$$

$$\Delta\eta = \eta_{j+1} - \eta_j \tag{39d}$$

The quantity $\hat{\mathbf{F}}$ denotes the flux normal to a cell-face, scaled such that

$$\hat{\mathbf{F}}d\eta = \mathbf{F}dy - \mathbf{G}dx\,. \tag{39e}$$

The analog of Equation 32e is

$$\hat{\mathbf{G}}_{i+\frac{1}{2},j}\Delta\xi = \frac{\mathbf{F}_{i,j}+\mathbf{F}_{i+1,j}}{2}\Delta_\xi y - \frac{\mathbf{G}_{i,j}+\mathbf{G}_{i+1,j}}{2}\Delta_\xi x \tag{40a}$$

with

$$\Delta_\xi x = x_{i+1,j} - x_{i,j} \tag{40b}$$

$$\Delta_\xi y = y_{i+1,j} - y_{i,j} \tag{40c}$$

$$\Delta\xi = \xi_{i+1} - \xi_i \tag{40d}$$

and

$$\hat{\mathbf{G}}d\xi = \mathbf{F}dy - \mathbf{G}dx\,. \tag{40e}$$

Since, in all but the simplest cases, the grid cells are not Cartesian, the Cartesian Courant numbers, ν_x and ν_y must be replaced with "contravariant Courant numbers." The contravariant Courant numbers ν_ξ and ν_η are related to the wave speeds normal to the cell faces. They are given by the formulas

$$(\nu_\xi)_{i+\frac{1}{2},j+\frac{1}{2}} = \frac{\Delta t}{A}\left(c_x\Delta_\eta y - c_y\Delta_\eta x\right)_{i+\frac{1}{2},j+\frac{1}{2}}\,, \tag{41a}$$

with

$$(\Delta_\eta x)_{i+\frac{1}{2},j+\frac{1}{2}} = \frac{1}{2}\left(x_{i,j+1} - x_{i,j} + x_{i+1,j+1} - x_{i+1,j}\right) \tag{41b}$$

$$(\Delta_\eta y)_{i+\frac{1}{2},j+\frac{1}{2}} = \frac{1}{2}\left(y_{i,j+1} - y_{i,j} + y_{i+1,j+1} - y_{i+1,j}\right)\,, \tag{41c}$$

and

$$(\nu_\eta)_{i+\frac{1}{2},j+\frac{1}{2}} = \frac{\Delta t}{A}\left(c_x\Delta_\xi y - c_y\Delta_\xi x\right)_{i+\frac{1}{2},j+\frac{1}{2}}\,, \tag{42a}$$

with

$$(\Delta_\xi x)_{i+\frac{1}{2},j+\frac{1}{2}} = \frac{1}{2}\left(x_{i+1,j} - x_{i,j} + x_{i+1,j+1} - x_{i,+1j}\right) \tag{42b}$$

$$(\Delta_\xi y)_{i+\frac{1}{2},j+\frac{1}{2}} = \frac{1}{2}\left(y_{i+1,j} - y_{i,j} + y_{i+1,j+1} - y_{i,j+1}\right)\,. \tag{42c}$$

The distribution step requires, in each cell, projection of the residual onto the columns of the matrix $\mathbf{P}^*$, giving weights $r^{(k)}$, and multiplication of each of the resulting vectors by an appropriate time-step:

$$\mathbf{Res}_{i+\frac{1}{2},j+\frac{1}{2}} = \sum_{k=1}^{4}\left(r^{(k)}\mathbf{P}^{*(k)}\right)_{i+\frac{1}{2},j+\frac{1}{2}} \tag{43a}$$

$$\delta_t\mathbf{U}^{(k)}_{i+\frac{1}{2},j+\frac{1}{2}} = \left(\Delta t^{(k)}r^{(k)}\mathbf{P}^{*(k)}\right)_{i+\frac{1}{2},j+\frac{1}{2}}\,, \tag{43b}$$

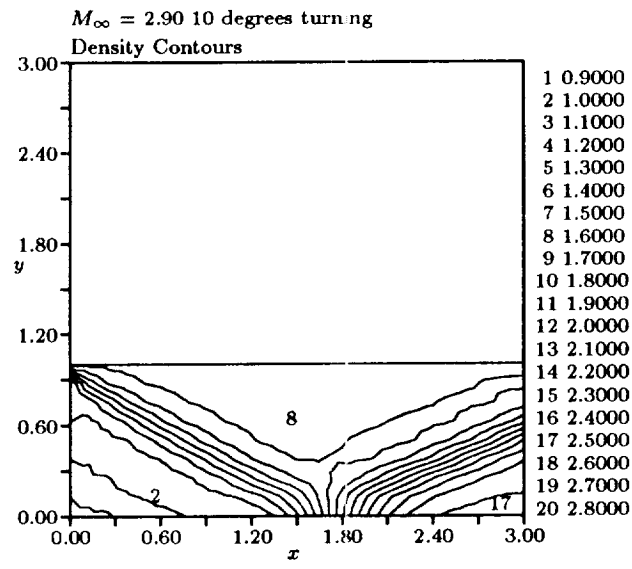

Figure 29: Downwind Distribution Scheme — 24 × 8 Grid

where k varies from one to four. In the above, $\mathbf{P}^{*(k)}$ denotes the k^{th} column of $\mathbf{P}^*$, corresponding to the k^{th} wave, and $\delta_t \mathbf{U}^{(k)}$ is the portion of time change in the state vector caused by the k^{th} wave. Each $\delta_t \mathbf{U}^{(k)}$ may be divided between the two vertices of the downwind cell-face, according to the weights of Equations 35a–35d, with ν_x and ν_y replaced by $\nu_\xi^{(k)}$ and $\nu_\eta^{(k)}$, e.g.

$$\omega_{ne}^{(k)} = \max\left(0, \frac{\left(\nu_\xi^{(k)} + \nu_\eta^{(k)}\right)}{|\nu_\xi^{(k)} + \nu_\eta^{(k)}| + |\nu_\xi^{(k)} - \nu_\eta^{(k)}|}\right) . \tag{44}$$

The wave speeds $c_x^{(k)}$ and $c_y^{(k)}$ arising in the calculation of $\nu_\xi^{(k)}$ and $\nu_\eta^{(k)}$ are the diagonal elements of $\mathbf{D}_x$ and $\mathbf{D}_y$, given in Section 2.

Results for this scheme are shown in Figures 29–32. The checkerboard instability permitted by the scheme can be seen in the odd-even decoupling that takes place upstream of the first shock. It was necessary to damp this mode with a nonlinear artificial viscosity of the type developed by Jameson *et al* [15]. To avoid random directions $\boldsymbol{\kappa}^{(1)}$ and $\boldsymbol{\kappa}^{(2)}$ in regions of small velocity and pressure gradients, both were taken to be along the flow direction in these regions. Despite this, the $\boldsymbol{\kappa}$ vectors are quite noisy, as can be seen in Figures 33 and 34. The overall results for this scheme are disappointing, in that they are almost indistinguishable from the results for second-order grid-aligned upwinding.

4 A Scheme Based on a Rotated Riemann Problem

In the second method, the pressure gradient angle θ_p, given by

$$\theta_p = \tan^{-1} \frac{\partial p / \partial y}{\partial p / \partial x} , \tag{45a}$$

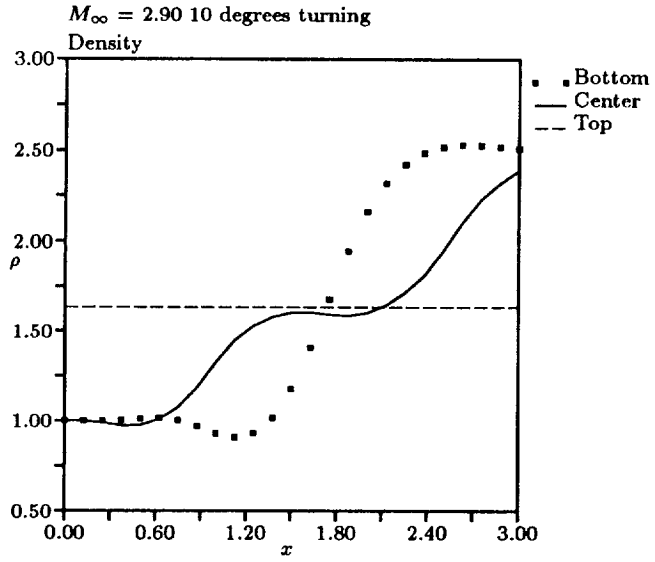

Figure 30: Downwind Distribution Scheme — 24 × 8 Grid

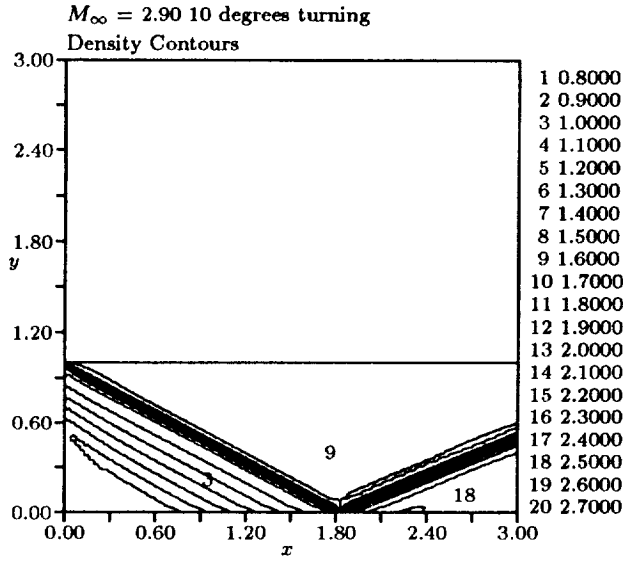

Figure 31: Downwind Distribution Scheme — 96 × 32 Grid

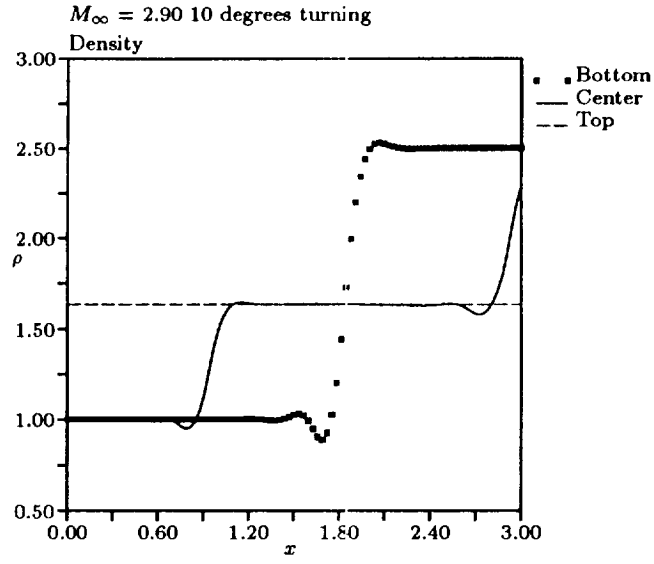

Figure 32: Downwind Distribution Scheme — 96 × 32 Grid

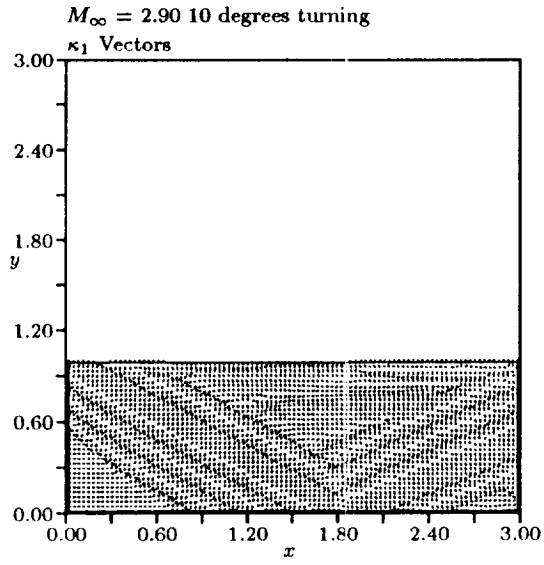

Figure 33: Downwind Distribution Scheme — $\kappa^{(1)}$ Vectors

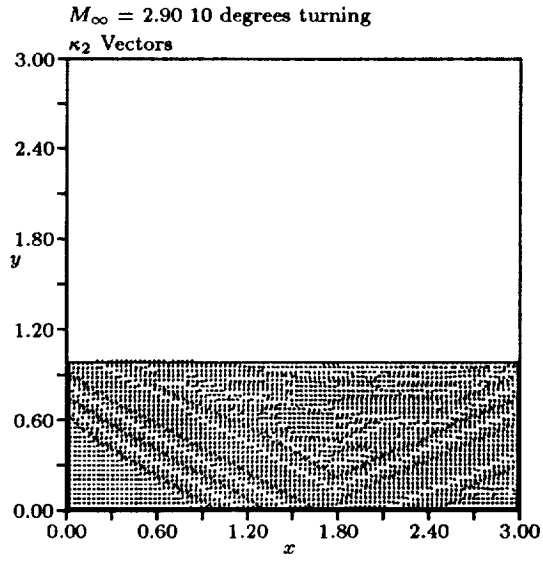

Figure 34: Downwind Distribution Scheme — $\kappa^{(2)}$ Vectors

is used to construct the dominant-direction angle. To avoid random angles in areas with small pressure gradients, the dominant-direction angle used is a blend of the pressure gradient angle with the flow angle, θ_s. The blending is accomplished by

$$\cos\theta = \frac{\epsilon\frac{|\nabla p|}{\rho a^2}\cos\theta_p + (1-\epsilon)\frac{|u|}{a}\cos\theta_s}{\epsilon\frac{|\nabla p|}{\rho a^2} + (1-\epsilon)\frac{|u|}{a}}, \tag{45b}$$

where a typical value is $\epsilon = 0.9$.

The generic fomula for a flux normal to a cell face is

$$\mathbf{F} = \mathbf{F}(\mathbf{U_L}, \mathbf{U_R}); \tag{46}$$

in a conventional first-order-scheme the left and right input states simply are the average values in the adjacent cells. Convection speeds are based on velocity components parallel and perpendicular to the cell face; the dominant direction, i.e., the direction in which the Riemann problem is solved, is normal to the cell face.

When a dominant direction is chosen that is not normal to the cell face, the flux component in this direction is

$$\mathbf{F}_\perp = \mathbf{F}_\perp(\mathbf{U}_{\mathbf{L}_\perp}, \mathbf{U}_{\mathbf{R}_\perp}). \tag{47}$$

This flux is computed as before, with two changes. The velocity components are now in the new reference frame (that is, the angle θ_g is replaced with the dominant-direction angle, θ), and the left and right states are interpolated from the values in the nearest cell centers, as shown in Figure 35. The subscript $\perp$ is chosen to indicate that the direction, although not normal to a cell face, may be normal to another important line, such as a shock front. For higher-order interpolation, a second "outer" ring of cells is also used, as shown in Figure 36.

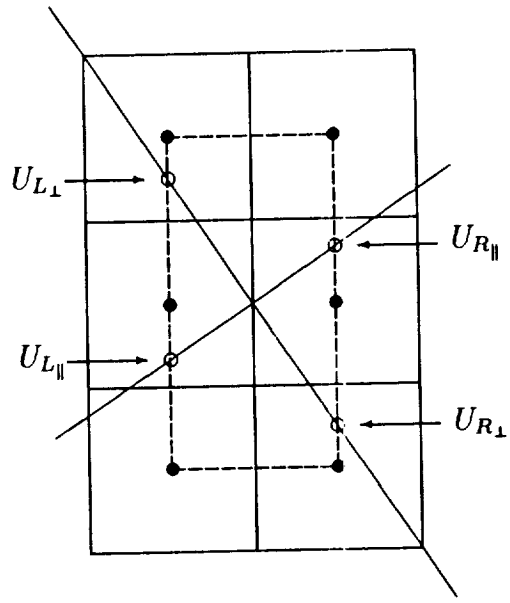

Figure 1: First-Order Interpolation for Rotated Riemann Solver Scheme

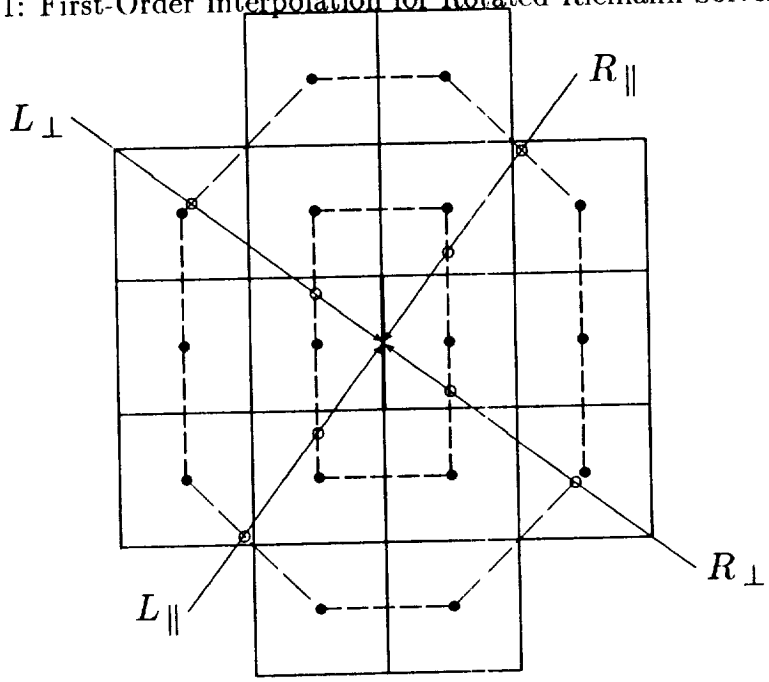

Figure 2: Second-Order Interpolation for Rotated Riemann Solver Scheme

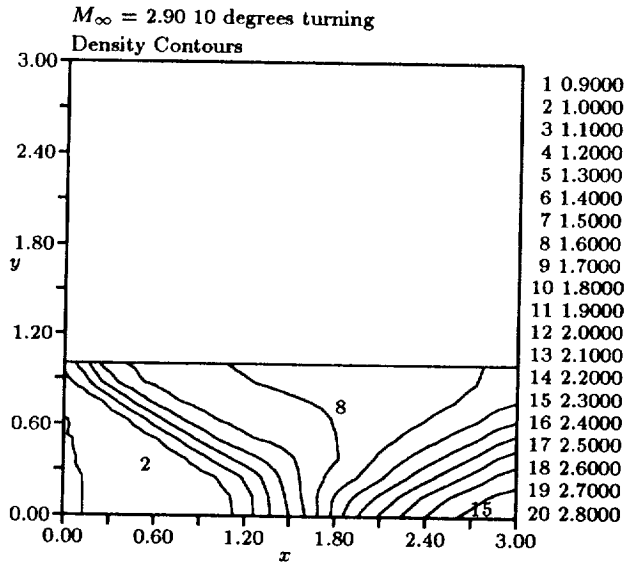

Figure 37: First-Order Scheme with Rotated Riemann Solver — 24 × 8 Grid

Next, a flux normal to this dominant direction,

$$\mathbf{F}_{\parallel} = \left(\mathbf{U}_{\mathbf{L}_{\parallel}}, \mathbf{U}_{\mathbf{R}_{\parallel}}\right), \tag{48}$$

must be calculated; the input states $\left(\mathbf{U}_{\mathbf{L}_{\parallel}}, \mathbf{U}_{\mathbf{R}_{\parallel}}\right)$ for this flux are also found by interpolation. Note that this flux component also exists in the conventional formulation, but does not contribute to the flux through the cell face.

The flux normal to the cell face is constructed by rotating the above fluxes back to the coordinate frame normal to the cell face:

$$\mathbf{F}\left(\mathbf{U}_{\mathbf{L}_{\perp}}, \mathbf{U}_{\mathbf{R}_{\perp}}, \mathbf{U}_{\mathbf{L}_{\parallel}}, \mathbf{U}_{\mathbf{R}_{\parallel}}\right) = \cos\left(\theta - \theta_g\right)\mathbf{F}_{\perp} - \sin\left(\theta - \theta_g\right)\mathbf{F}_{\parallel}. \tag{49}$$

Here, θ is the dominant-direction angle and θ_g is the angle of the normal to the cell face (the "grid angle").

Because of the necessity of both a "parallel" and a "perpendicular" flux function, this scheme corresponds to using an eight-wave model for the fluid interaction at each interface.

Results for the first-order scheme are shown in Figures 37–40. Results for the second-order scheme are shown in Figures 41–44. Comparison with the results of the grid-aligned scheme (Figures 6–13) shows a substantial improvement for the first-order scheme, but a less noticeable improvement for the second-order scheme. The dominant-direction vectors are shown in Figure 45. Away from the shocks, the angle is in the flow direction. In the vicinity of the shocks, it is normal to the shocks.

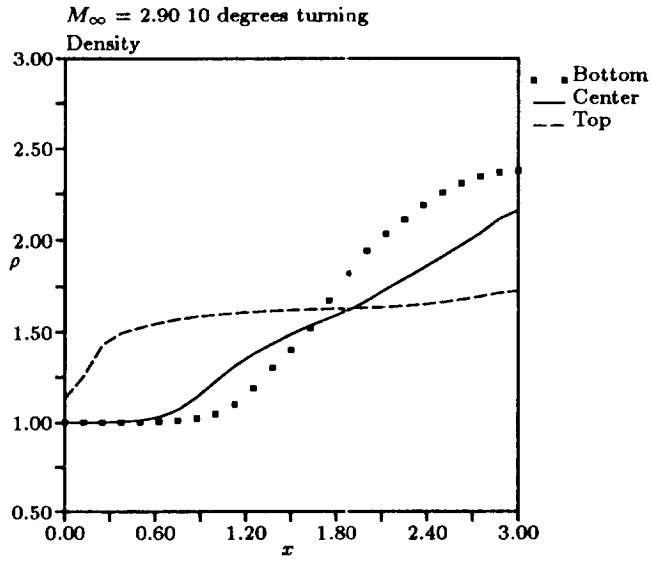

Figure 38: First-Order Scheme with Rotated Riemann Solver — 24 × 8 Grid

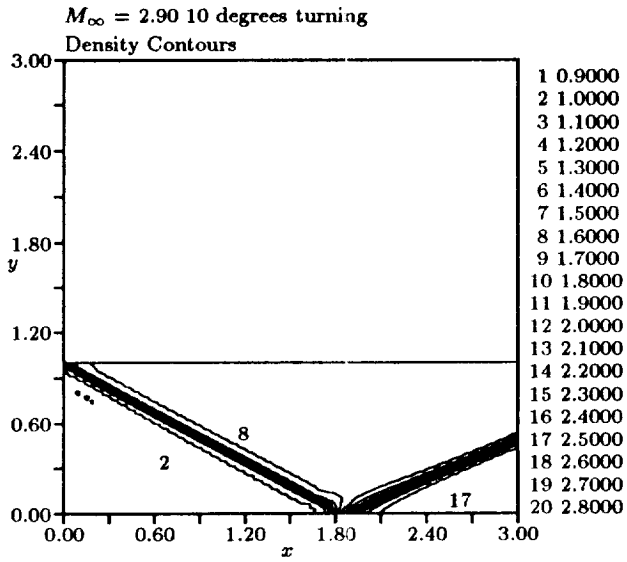

Figure 39: First-Order Scheme with Rotated Riemann Solver — 96 × 32 Grid

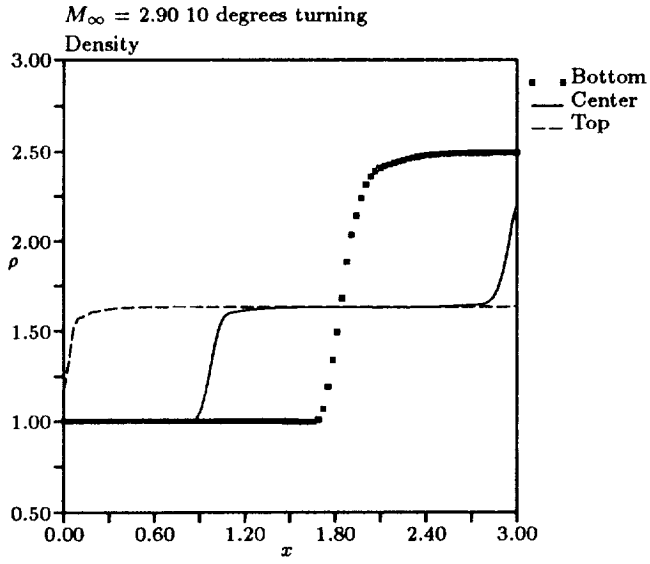

Figure 40: First-Order Scheme with Rotated Riemann Solver — 96 × 32 Grid

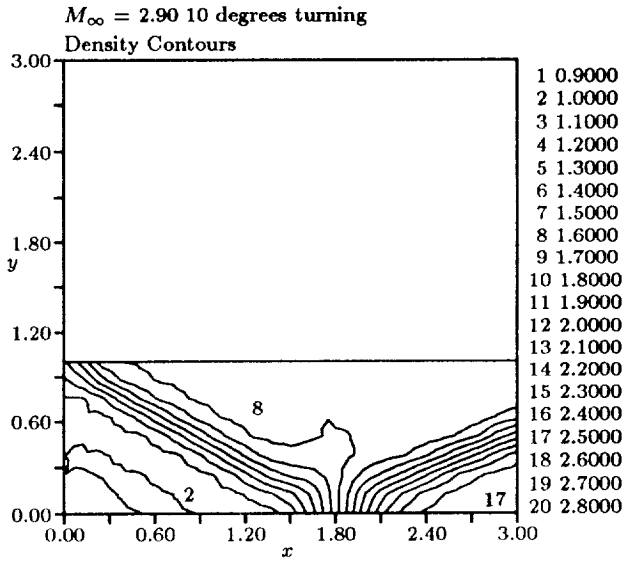

Figure 41: Second-Order Scheme with Rotated Riemann Solver — 24 × 8 Grid

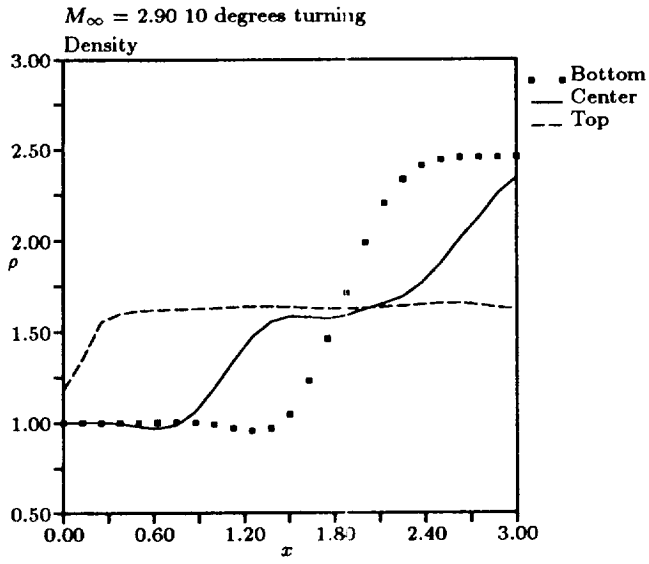

Figure 42: Second-Order Scheme with Rotated Riemann Solver — 24 × 8 Grid

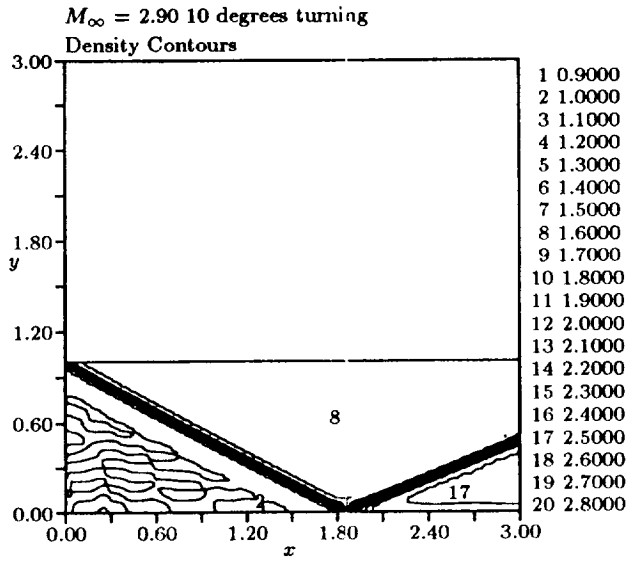

Figure 43: Second-Order Scheme with Rotated Riemann Solver — 96 × 32 Grid

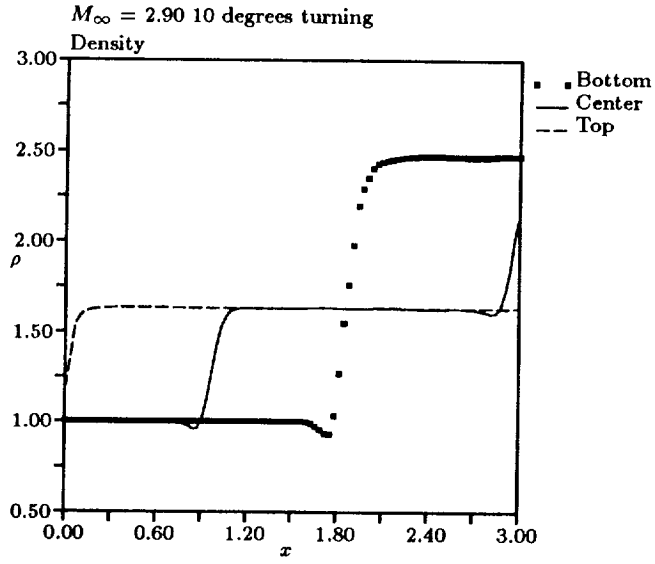

Figure 44: Second-Order Scheme with Rotated Riemann Solver — 96 × 32 Grid

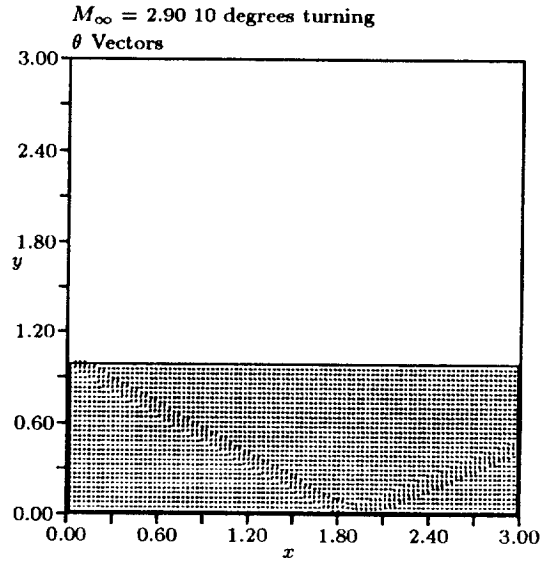

Figure 45: Second-Order Scheme with Rotated Riemann Solver — Upwinding Directions

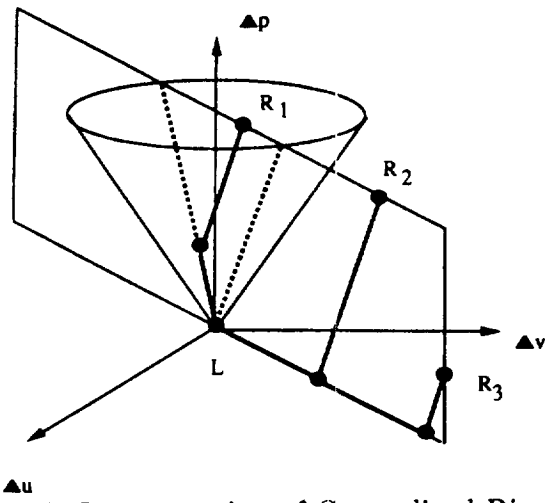

Figure 46: Geometric Interpretation of Generalized Riemann Solver

5 A Scheme Based on a Generalized Riemann Solver

The third scheme is based on the velocity-difference direction

$$\theta = \tan^{-1}\left(\frac{v_R - v_L}{u_R - u_L}\right). \tag{50}$$

Depending on the relative magnitudes of the pressure difference and velocity difference, the difference between the two states $\tilde{\mathbf{U}}_\mathbf{L}$ and $\tilde{\mathbf{U}}_\mathbf{R}$ is broken down into different combinations of waves:

- if
$$\Delta p \geq \hat{\rho}\hat{c}\sqrt{(\Delta u)^2 + (\Delta v)^2},$$
two acoustic waves and one entropy wave all running in the θ-direction;

- if
$$\Delta p < \hat{\rho}\hat{c}\sqrt{(\Delta u)^2 + (\Delta v)^2},$$
one acoustic wave and one entropy wave running in the θ-direction, plus one shear wave running in the direction $\theta + \pi/2$.

The idea behind this approach can be seen graphically in Figure 46. The axes in the figure are the velocity differences Δu and Δv, and the pressure difference Δp. The left state, $\tilde{\mathbf{U}}_\mathbf{L}$, is at the origin. For a right state $\tilde{\mathbf{U}}_\mathbf{R}$ inside the cone, such as $\tilde{\mathbf{U}}_{\mathbf{R}_1}$, the pressure difference is dominant, and the difference between $\tilde{\mathbf{U}}_\mathbf{L}$ and $\tilde{\mathbf{U}}_\mathbf{R}$ is described as two acoustic waves (the entropy wave, corresponding to a difference in density between the two states, is not shown in the figure). For a right state $\tilde{\mathbf{U}}_\mathbf{R}$ outside the cone, such as $\tilde{\mathbf{U}}_{\mathbf{R}_2}$ or $\tilde{\mathbf{U}}_{\mathbf{R}_3}$, the difference between the left and right states is described by one acoustic wave and one shear wave. The shear waves show up as lines in the (Δu, Δv) plane (no pressure difference); the acoustic waves show up as lines parallel to the rays generating the cone.

In practice the scheme has to be slightly elaborated, because nonlinear feedback makes it necessary to "freeze" the angle θ over many interations. If the latest frozen value is θ_1, an additional weak shear wave connects $\tilde{\mathbf{U}}_\mathbf{R}$ to the plane representing the θ_1-direction. This

shear wave moves in the θ_1 direction; its graphical representation is a line segment in the direction $\theta_1 + \pi/2$, connecting the θ-plane in the figure to the "frozen" θ_1 plane.

The first step of the scheme is to determine which set of waves to use. In the case

$$\left|\frac{\Delta p}{\hat{\rho}\hat{c}^2}\right| < \left|\frac{1}{\hat{c}}\sqrt{(\Delta u)^2 + (\Delta v)^2}\cos(\theta - \theta_1)\right|, \tag{51a}$$

one acoustic wave, two shear waves and one entropy wave are used. In the sub-case

$$\Delta p \cos(\theta - \theta_1) < 0 \tag{51b}$$

an acoustic wave of the first type is used; in the sub-case

$$\Delta p \cos(\theta - \theta_1) \geq 0 \tag{51c}$$

an acoustic wave of the second type is used. In the case

$$\left|\frac{\Delta p}{\hat{\rho}\hat{c}^2}\right| \geq \left|\frac{1}{\hat{c}}\sqrt{(\Delta u)^2 + (\Delta v)^2}\cos(\theta - \theta_1)\right|, \tag{51d}$$

two acoustic waves, a shear wave and an entropy wave are used.

The interface fluxes are then calculated as for Roe's scheme, with

$$\mathbf{F}(\mathbf{U_L}, \mathbf{U_R}) = \frac{1}{2}(\mathbf{F_L} + \mathbf{F_R}) - \frac{1}{2}\sum_{k=1}^{4}\left|\hat{\lambda}_k\right|\Delta V_k \hat{\mathbf{R}}_k, \tag{52}$$

with the definitions of the wave parameters depending on which model is used.

For the case of two acoustic waves, a shear wave and an entropy wave, the eigenvectors are given by

$$\hat{\mathbf{R}}_1 = \begin{pmatrix} 1 \\ \hat{u} - \hat{c}\cos\theta_1 \\ \hat{v} - \hat{c}\sin\theta_1 \\ \hat{h_0} - \hat{c}(\hat{u}\cos\theta_1 + \hat{v}\sin\theta_1) \end{pmatrix}, \tag{53a}$$

$$\hat{\mathbf{R}}_2 = \begin{pmatrix} 0 \\ -\sin\theta_1 \\ \cos\theta_1 \\ (\hat{v}\cos\theta_1 - \hat{u}\sin\theta_1) \end{pmatrix}, \tag{53b}$$

$$\hat{\mathbf{R}}_3 = \begin{pmatrix} 1 \\ \hat{u} \\ \hat{v} \\ \frac{1}{2}(\hat{u}^2 + \hat{v}^2) \end{pmatrix}, \tag{53c}$$

$$\hat{\mathbf{R}}_4 = \begin{pmatrix} 1 \\ \hat{u} + \hat{c}\cos\theta_1 \\ \hat{v} + \hat{c}\sin\theta_1 \\ \hat{h}_0 + \hat{c}\,(\hat{u}\cos\theta_1 + \hat{v}\sin\theta_1) \end{pmatrix}. \tag{53d}$$

The wave strengths for this case are given by

$$\Delta V_1 = \frac{1}{2\hat{c}^2}\left(\Delta p - \hat{\rho}\hat{c}\sqrt{(\Delta u)^2 + (\Delta v)^2}\cos(\theta - \theta_1)\right) \tag{54a}$$

$$\Delta V_2 = \hat{\rho}\sqrt{(\Delta u)^2 + (\Delta v)^2}\sin(\theta - \theta_1) \tag{54b}$$

$$\Delta V_3 = \Delta\rho - \frac{1}{\hat{c}^2}\Delta p \tag{54c}$$

$$\Delta V_4 = \frac{1}{2\hat{c}^2}\left(\Delta p + \hat{\rho}\hat{c}\sqrt{(\Delta u)^2 + (\Delta v)^2}\cos(\theta - \theta_1)\right) \tag{54d}$$

and the wave speeds by

$$\hat{\lambda}_1 = (\hat{u}\cos\theta_1 + \hat{v}\sin\theta_1 - \hat{c})\cos(\theta_1 - \theta_g) \tag{55a}$$

$$\hat{\lambda}_2 = (\hat{u}\cos\theta_1 + \hat{v}\sin\theta_1)\cos(\theta_1 - \theta_g) \tag{55b}$$

$$\hat{\lambda}_3 = (\hat{u}\cos\theta_1 + \hat{v}\sin\theta_1)\cos(\theta_1 - \theta_g) \tag{55c}$$

$$\hat{\lambda}_4 = (\hat{u}\cos\theta_1 + \hat{v}\sin\theta_1 + \hat{c})\cos(\theta_1 - \theta_g) \tag{55d}$$

where θ_g is the "grid angle," i.e. the angle of the normal to the interface. In these speeds, the projection onto the interface normal has been taken into account.

For the case of an acoustic wave of the first type, two shear waves and an entropy wave, the vectors are given by

$$\hat{\mathbf{R}}_1 = \begin{pmatrix} 1 \\ \hat{u} - \hat{c}\cos\theta_1 \\ \hat{v} - \hat{c}\sin\theta_1 \\ \hat{h}_0 - \hat{c}\,(\hat{u}\cos\theta_1 + \hat{v}\sin\theta_1) \end{pmatrix}, \tag{56a}$$

$$\hat{\mathbf{R}}_2 = \begin{pmatrix} 0 \\ -\sin\theta_1 \\ \cos\theta_1 \\ (\hat{v}\cos\theta_1 - \hat{u}\sin\theta_1) \end{pmatrix}, \tag{56b}$$

$$\hat{\mathbf{R}}_3 = \begin{pmatrix} 1 \\ \hat{u} \\ \hat{v} \\ \frac{1}{2}(\hat{u}^2 + \hat{v}^2) \end{pmatrix}, \tag{56c}$$

$$\hat{\mathbf{R}}_4 = \begin{pmatrix} 0 \\ -\cos\theta_1 \\ -\sin\theta_1 \\ -(\hat{v}\sin\theta_1 + \hat{u}\cos\theta_1) \end{pmatrix}. \tag{56d}$$

The wave strengths for this case are given by

$$\Delta V_1 = \frac{\Delta p}{\hat{c}^2} \tag{57a}$$

$$\Delta V_2 = \hat{\rho}\sqrt{(\Delta u)^2 + (\Delta v)^2}\sin(\theta - \theta_1) \tag{57b}$$

$$\Delta V_3 = \Delta\rho - \frac{1}{\hat{c}^2}\Delta p \tag{57c}$$

$$\Delta V_4 = \frac{1}{\hat{c}}\left(-\Delta p - \hat{\rho}\hat{c}\sqrt{(\Delta u)^2 + (\Delta v)^2}\cos(\theta - \theta_1)\right) \tag{57d}$$

and the wave speeds by

$$\hat{\lambda}_1 = (\hat{u}\cos\theta_1 + \hat{v}\sin\theta_1 - \hat{c})\cos(\theta_1 - \theta_g) \tag{58a}$$

$$\hat{\lambda}_2 = (\hat{u}\cos\theta_1 + \hat{v}\sin\theta_1)\cos(\theta_1 - \theta_g) \tag{58b}$$

$$\hat{\lambda}_3 = (\hat{u}\cos\theta_1 + \hat{v}\sin\theta_1)\cos(\theta_1 - \theta_g) \tag{58c}$$

$$\hat{\lambda}_4 = (\hat{u}\sin\theta_1 - \hat{v}\cos\theta_1)\sin(\theta_1 - \theta_g)\,. \tag{58d}$$

For the case of an acoustic wave of the second type, two shear waves and an entropy wave, the vectors are given by

$$\hat{\mathbf{R}}_1 = \begin{pmatrix} 0 \\ -\cos\theta_1 \\ -\sin\theta_1 \\ -(\hat{v}\sin\theta_1 + \hat{u}\cos\theta_1) \end{pmatrix}, \tag{59a}$$

$$\hat{\mathbf{R}}_2 = \begin{pmatrix} 0 \\ -\sin\theta_1 \\ \cos\theta_1 \\ (\hat{v}\cos\theta_1 - \hat{u}\sin\theta_1) \end{pmatrix}, \tag{59b}$$

$$\hat{\mathbf{R}}_3 = \begin{pmatrix} 1 \\ \hat{u} \\ \hat{v} \\ \frac{1}{2}(\hat{u}^2 + \hat{v}^2) \end{pmatrix}, \tag{59c}$$

$$\hat{\mathbf{R}}_4 = \begin{pmatrix} 1 \\ \hat{u} + \hat{c}\cos\theta_1 \\ \hat{v} + \hat{c}\sin\theta_1 \\ \hat{h_0} + \hat{c}(\hat{u}\cos\theta_1 + \hat{v}\sin\theta_1) \end{pmatrix}. \tag{59d}$$

The wave strengths for this case are given by

$$\Delta V_1 = \frac{1}{\hat{c}}\left(\Delta p - \hat{\rho}\hat{c}\sqrt{(\Delta u)^2 + (\Delta v)^2}\cos(\theta - \theta_1)\right) \tag{60a}$$

$$\Delta V_2 = \hat{\rho}\sqrt{(\Delta u)^2 + (\Delta v)^2}\sin(\theta - \theta_1) \tag{60b}$$

$$\Delta V_3 = \Delta\rho - \frac{1}{\hat{c}^2}\Delta p \tag{60c}$$

$$\Delta V_4 = \frac{\Delta p}{\hat{c}^2} \tag{60d}$$

and the wave speeds by

$$\hat{\lambda}_1 = (\hat{u}\sin\theta_1 - \hat{v}\cos\theta_1)\sin(\theta_1 - \theta_g) \tag{61a}$$

$$\hat{\lambda}_2 = (\hat{u}\cos\theta_1 + \hat{v}\sin\theta_1)\cos(\theta_1 - \theta_g) \tag{61b}$$

$$\hat{\lambda}_3 = (\hat{u}\cos\theta_1 + \hat{v}\sin\theta_1)\cos(\theta_1 - \theta_g) \tag{61c}$$

$$\hat{\lambda}_4 = (\hat{u}\cos\theta_1 + \hat{v}\sin\theta_1 + \hat{c})\cos(\theta_1 - \theta_g)\,. \tag{61d}$$

As in the standard grid-aligned scheme, the difference between two states is described in terms of four waves. In this scheme, however, the choice of waves depends on the relative magnitudes of the pressure difference and velocity difference between the states.

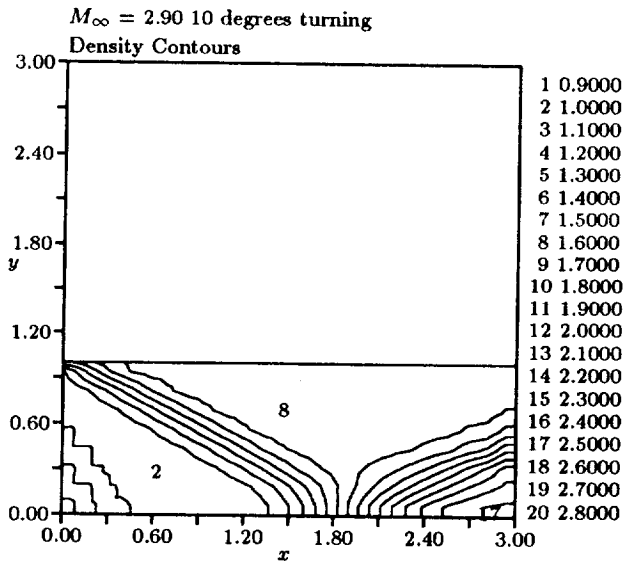

Figure 47: First-Order Scheme with Generalized Riemann Solver — 24 × 8 Grid

Results for this scheme are shown in Figures 47–50. They show a substantial improvement over the first-order grid-aligned results (Figures 6–9), and a slight improvement over the second-order grid-aligned results (Figures 6–9).

Further development of the generalized Riemann solver must be aimed at making it more robust, without giving up its resolving power. A promising approach, currently being investigated, is to "anchor" the wave decomposition to the frame of the local flow direction; this is accomplished by simply taking θ_1 equal to the flow angle. For normal, or almost normal, shocks, the results remain grid-independent; for more oblique shocks, resolution is lost because the flow direction is not a good indicator of the shock normal, and some weight should be given to the velocity-difference direction. This can be done by explaining part of the jump between $\mathbf{U}_L$ and $\mathbf{U}_R$ by the generalized Riemann solver based on the velocity-difference direction, and the remainder by the generalized Riemann solver based on the streamwise direction. The full flux calculation then involved seven waves.

6 An Outlook for Multi-Dimensional Upwind Schemes

The outlook for genuinely multi-dimensional upwind schemes is still clouded. For the reflected shock cases presented here, all schemes tested showed improvements over first-order grid-aligned schemes, but the improvements over second-order grid-aligned were very slight. It is not clear whether this result is a condemnation of multi-dimensional schemes, or a confirmation of grid-aligned schemes. The improvements over grid-aligned upwinding do come at a cost of complexity and convergence.

The downwind distribution scheme fundamentally differs from the other two schemes presented here: it is a cell-vertex scheme. This implies better accuracy on stretched meshes, and a simpler extension to unstructured meshes than for the cell-centered schemes. However,

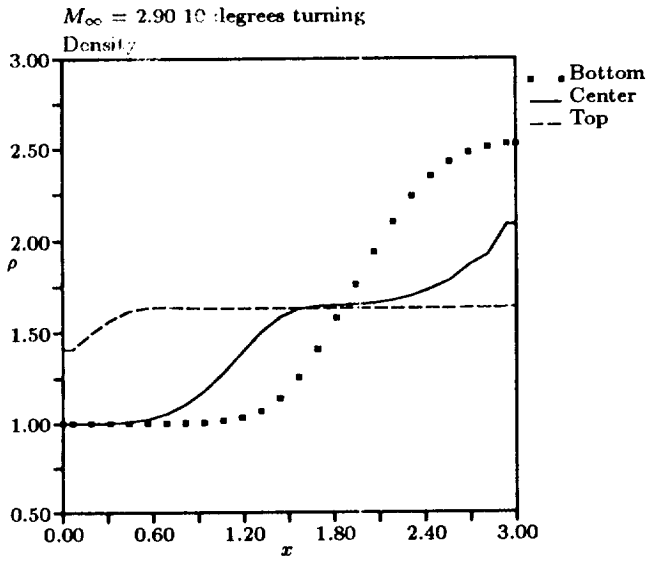

Figure 48: First-Order Scheme with Generalized Riemann Solver — 24 × 8 Grid

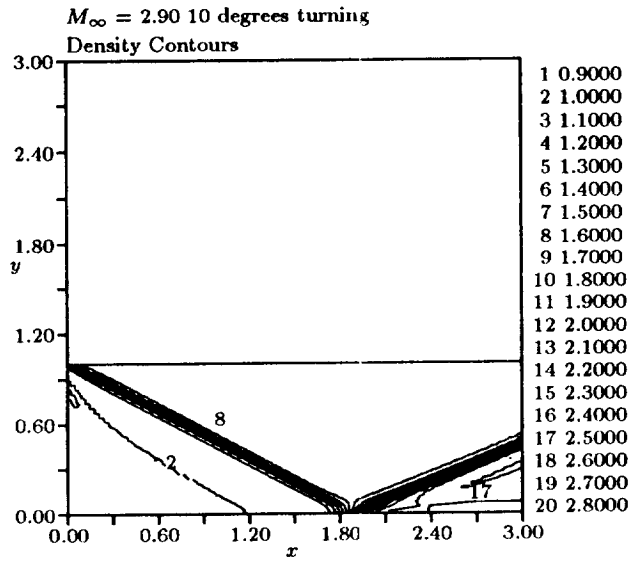

Figure 49: First-Order Scheme with Generalized Riemann Solver — 96 × 32 Grid

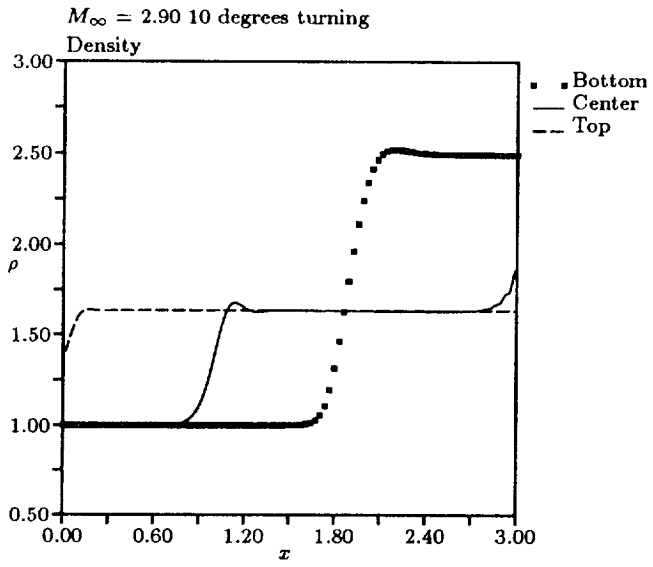

Figure 50: First-Order Scheme with Generalized Riemann Solver — 96 × 32 Grid

this scheme is also the least diffusive of the three, and the only one requiring additional damping to reach a converged steady state. There are also some difficulties associated with propagation directions that lie along grid lines. The random-distribution method presented here might alleviate these problems, but it relies on the fact that the cell-centered residuals, and not just the changes at the nodes, are zero when the steady state is reached. This may not be generally true; non-zero cell residuals could add up, in the distribution step, to give zero changes at the nodes. If this is the case, the random distribution scheme might not lead to convergence, or to the proper steady state.

The scheme based on a rotated Riemann solver is the most robust of the three schemes. Its cost, however, is fairly high. At each interface, almost twice the work of a grid-aligned Riemann solver is necessary to calculate the fluxes. Furthermore, the interpolation of the state vectors has an associated cost, both in computational work and in added storage. In three dimensions, the added storage could be prohibitive. The interpolation technique would be cumbersome on an unstructured grid.

The scheme based on a generalized Riemann solver seems, at this point in time, the most promising of the three approaches. The computational work for the scheme as outlined is only slightly more than that of a grid-aligned scheme. The nonlinearity added by basing the scheme on an angle calculated from local flow variables is detrimental to convergence, but ways to get around this are being developed. In one approach, a portion of the difference between the left and right states (approximately one-half) is decomposed according to the generalized Riemann solver, and the remainder is decomposed according to a stream-aligned Riemann solver. This approach, however, adds to the cost of the flux computation, approximately doubling it.

Clearly, the simple shock-reflection problem used in this paper cannot truly test these multi-dimensional schemes. More sophisticated problems, particularly ones in which shear

layers lie oblique to the grid, must be studied. Also, the possible range of schemes based on multi-dimensional ideas has not nearly been covered yet. For a topic in which research has begun only recently, though, the results are promising.

7 Acknowledgements

Many of the ideas and much of the work presented in this paper are attributable to Chris Rumsey, David Levy and Greg Ashford, all doctoral candidates working under the supervision of the authors. The work herein was funded by NASA Langley Research Center, the National Science Foundation and the McDonnell Aircraft Company.

References

[1] B. van Leer, J. L. Thomas, P. L. Roe, and R. W. Newsome, "A comparison of numerical flux formulas for the Euler and Navier-Stokes equations," in *AIAA 8th Computational Fluid Dynamics Conference*, 1987.

[2] P. L. Roe, "Approximate Riemann solvers, parameter vectors and difference schemes," *Journal of Computational Physics*, vol. 43, 1981.

[3] P. L. Roe, "Discrete models for the numerical analysis of time-dependent multidimensional gas-dynasmics," *Journal of Computational Physics*, vol. 63, 1986.

[4] C. Hirsch, C. Lacor, and H. Deconinck, "Convection algorithm based on a diagonalization procedure for the multidimensional Euler equations," in *AIAA 8th Computational Fluid Dynamics Conference*, 1987.

[5] H. Deconinck, C. Hirsch, and J. Peuteman, "Characteristic decomposition methods for the multidimensional Euler equations," *Lectures Notes in Physics*, vol. 264, 1987.

[6] H. Deconinck. Private Communication, 1989.

[7] D. Kröner, "Numerical schemes for the Euler equations in two space dimensions without dimensional splitting," in *Proceedings of the 2nd Conference on Hyperbolic Problems*, 1988.

[8] K. G. Powell and B. van Leer, "A genuinely multi-dimensional upwind cell-vertex scheme for the Euler equations," AIAA Paper 89-0095, 1989.

[9] R. Struijs and H. Deconinck, "A multidimensional upwind scheme for the Euler equations using fluctuation distribution on a grid consisting of triangles." Submitted for the Eighth GAMM Conference, Delft, 1989.

[10] C. Hirsch and C. Lacor, "Upwind algorithms based on a diagonalization of the multidimensional Euler equations," AIAA Paper 89-1958, 1989.

[11] M. B. Giles, W. K. Anderson, and T. W. Roberts, "Upwind control volumes: A new upwind approach," AIAA Paper 90-0104, 1990.

[12] A. Jameson, "Iterative solution of transonic flows over airfoils and wings," *Communications on Pure and Applied Mathematics*, vol. 28, 1974.

[13] S. F. Davis, "A rotationally-biased upwind difference scheme for the Euler equations," *Journal of Computational Physics*, vol. 56, 1984.

[14] D. Levy, K. G. Powell, and B. van Leer, "Implementation of a grid-independent upwind scheme for the Euler equations," in *AIAA 9th Computational Fluid Dynamics Conference*, 1989.

[15] A. Jameson, W. Schmidt, and E. Turkel, "Numerical solutions of the Euler equations by a finite-volume method using Runge-Kutta time-stepping schemes," AIAA Paper 81-1259, 1981.